Maximum-likelihood approach to strain imaging using ultrasound

M. F. Insana,[a] L. T. Cook, M. Bilgen, P. Chaturvedi, and Y. Zhu
Department of Radiology, University of Kansas Medical Center, 3901 Rainbow Boulevard, Kansas City, Kansas 66160-7234

(Received 4 January 1999; revised 8 September 1999; accepted 19 November 1999)

A maximum-likelihood (ML) strategy for strain estimation is presented as a framework for designing and evaluating bioelasticity imaging systems. Concepts from continuum mechanics, signal analysis, and acoustic scattering are combined to develop a mathematical model of the ultrasonic waveforms used to form strain images. The model includes three-dimensional (3-D) object motion described by affine transformations, Rayleigh scattering from random media, and 3-D system response functions. The likelihood function for these waveforms is derived to express the Fisher information matrix and variance bounds for displacement and strain estimation. The ML estimator is a generalized cross correlator for pre- and post-compression echo waveforms that is realized by waveform warping and filtering prior to cross correlation and peak detection. Experiments involving soft tissuelike media show the ML estimator approaches the Cramér–Rao error bound for small scaling deformations: at 5 MHz and 1.2% compression, the predicted lower bound for displacement errors is 4.4 μm and the measured standard deviation is 5.7 μm. [S0001-4966(00)00903-6]

PACS numbers: 43.60.Cg, 43.60.Gk, 43.80.Vj [JCB]

INTRODUCTION

Bioelasticity imaging provides important diagnostic information about soft tissue stiffness not available with other imaging modalities. It is based on the principles of manual palpation, a standard diagnostic technique, but promises greater sensitivity and spatial resolution. Numerous approaches to bioelasticity imaging have been proposed.[1–23] A common feature of each technique is a force that is carefully selected to displace the tissue in a way that can be tracked using standard imaging technology, often ultrasonics or magnetic resonance. Analysis of the estimated displacement field yields an image of an elasticity modulus or strain.

We study strain estimation from tissue displacements caused by *static* compression. Static compression minimizes the viscous effects of tissue dynamics. Local displacements are detected from changes in the ultrasonic echo fields recorded before and after compression. Unfortunately, the object motion necessary for strain contrast also can produce noise as coherence is reduced between waveforms recorded before and after compression. The performance of strain imaging for visualizing stiffness variations is often noise limited.

In a typical two-dimensional (2-D) strain imaging experiment, we confine all motion in the body to the image plane. We then scan the tissue with broadband pulse-echo ultrasound to record a radio-frequency echo field at high spatial resolution from the region of interest. This precompression echo field is a reference by which the position of scatterers after compression can be compared. Next we compress, hold, and re-scan the tissue to record the position of displaced scatterers. The displacement field is measured from the pre- and post-compression echo fields using a sequence of signal processing techniques that varies with the presumed nature of the deformation. Gradients of displacement are estimates of strain tensor components.[24] One primary objective of the image formation algorithm is to maximize coherence between the pre- and post-compression waveforms to be cross correlated.

When object deformation is accurately described by scaling spatial coordinates of the echo signal, then waveform *companding* applied before 1-D cross correlation has been found to produce low-noise time delay estimates[25] and strain images.[26] More complex deformations require image filtering[27] or warping[28,29] techniques to improve coherence at the expense of processing time. For very complex motions, compressions must be applied incrementally and accumulated to avoid waveform decorrelation.[11,30] We will show that a maximum-likelihood approach to displacement estimation can be implemented for strain imaging through least-squares techniques.

The amount of compression we apply depends on our ability to balance the requirements for (a) high coherence between pre- and post-compression echo fields, (b) accurate displacement estimation, and (c) high strain contrast between background and targets. Large compressions increase object contrast for strain but decrease waveform coherence particularly if cross correlation is the only displacement estimator. We also know from experience that choosing a compressor geometry and boundary restraints that yield a uniform stress field in the medium being imaged reduces decorrelation errors and simplifies the resulting strain patterns. The challenge for designing bioelasticity imaging systems is to control a large number of coupled variables that influence task

[a]Current address: Biomedical Engineering, University of California, One Shields Avenue, Davis, CA 95616. Electronic mail: mfinsana@ucdavis.edu

performance. Yet most of what is known about strain imaging is empirical.

An excellent introduction to signal analysis for motion estimation in bioelasticity imaging is found in the extensive literature on time delay estimation for sonar and radar[31,32] and for blood velocity estimation.[33,34] These works explore velocity and range estimation for spread target, spread velocity situations using wide-band signals (total bandwidths between 20% and 100%). Our study extends the conditions by analyzing wide-band maximum-likelihood estimation of slowly fluctuating (i.e., strain constant over a pulse volume) spread targets that move in a plane or volume.

Specifically, this paper investigates a maximum-likelihood approach to displacement and strain estimation to provide a rigorous strategy for designing and evaluating strain image formation algorithms and instrumentation. The goals are to find principles that guide experimental design and predict error bounds. Our viewpoint is from the traditional time-delay estimation literature where much is known about motion detection, albeit largely in one dimension and without signal decorrelation. We first describe a comprehensive ultrasonic waveform model that includes deformation of the scattering medium consistent with static compression of biological tissues. Second, the concept of coherence is developed for strain imaging. Coherence is at the core of algorithm design and performance assessment. Third, the maximum-likelihood strategy for displacement estimation is developed. Fourth, error bounds for displacement and strain estimates are found, verified with simulation, and compared with phantom experiments. The results are a rigorous framework for future developments of strain imaging using ultrasound.

I. ULTRASONIC WAVEFORM MODEL

We model an ultrasonic echo waveform $r(\mathbf{x})$ as the sum of a random process $\overline{r}(\mathbf{x})$, which we refer to as the noise-free echo signal, and a signal-independent noise process $n(\mathbf{x})$. Each is a function of position (boldface) $\mathbf{x}=(x_1,x_2,x_3)^t$, a vector of Euclidean 3-space. The transpose of $\mathbf{x}$ is indicated by $\mathbf{x}^t$. For incident plane waves and far-field observation, it is well known that the scattered pressure from a random medium is the sum of spherically diverging waves.[35] However, modeling echo signals recorded during a pulse-echo experiment requires that we also include the point-spread function for the imaging system.

A. Echo signals

An echo signal may be described as a function of the scattering amplitude $\Phi(\mathbf{u})$ and pulse-echo transfer function $\tilde{H}(\mathbf{u})$[36] at spatial frequency $\mathbf{u}$,[37]

$$\overline{r}(\mathbf{x})=\mathcal{F}^{-1}\{\tilde{H}(\mathbf{u})\Phi(\mathbf{u})\}, \tag{1}$$

where $\mathcal{F}\{\tilde{h}(\mathbf{x})\}=\tilde{H}(\mathbf{u})$ is the forward 3-D Fourier transform of the pulse-echo point-spread function $\tilde{h}(\mathbf{x})$ and $\mathcal{F}^{-1}\{\tilde{H}(\mathbf{u})\}=\tilde{h}(\mathbf{x})$ is its inverse.

The amount of acoustic energy scattered depends on the microscopic distribution of three coupled tissue properties: mass density $\rho(\mathbf{x})$, bulk compressibility $\kappa(\mathbf{x})$, and specific acoustic impedance $z(\mathbf{x})$. For local plane waves $z(\mathbf{x})=\pm\sqrt{\rho(\mathbf{x})/\kappa(\mathbf{x})}$. Specifically, the scattering amplitude describes a spatial-frequency distribution of scattered energy from the random *spatial fluctuations* in mass density $\Delta\rho(\mathbf{x})/\rho(\mathbf{x})$, compressibility $\Delta\kappa(\mathbf{x})/\kappa_0$, and impedance $\Delta z(\mathbf{x})/z_0$ according to[35,38]

$$\begin{aligned}\Phi(\mathbf{u})&=\pi u_1^2\mathcal{F}\left\{\frac{\Delta\kappa(\mathbf{x})}{\kappa_0}-\frac{\Delta\rho(\mathbf{x})}{\rho(\mathbf{x})}\right\}\\&=-2\pi u_1^2\mathcal{F}\left\{\frac{\Delta z(\mathbf{x})}{z_0}\right\}=\frac{1}{2\pi z_0}\mathcal{F}\left\{\frac{\partial^2 z(\mathbf{x})}{\partial x_1^2}\right\}.\end{aligned} \tag{2}$$

The spatial-frequency component u_1 corresponds to the spatial coordinate parallel to the axis of the ultrasound beam x_1, and κ_0 and z_0 are the spatial averages of the corresponding quantities. To find the final form of Eq. (2), we used the relation $\Delta\kappa(\mathbf{x})/\kappa_0-\Delta\rho(\mathbf{x})/\rho(\mathbf{x})=-2\Delta z(\mathbf{x})/z_0$ and the derivative theorem for Fourier transforms.[39] The equation shows that sound is scattered wherever the second derivative of the acoustic impedance in the direction of the transmitted beam axis is nonzero. Scattering may be considered as a high-pass filter of the object function z, attenuation as a low-pass filter, and the point-spread function as a band-pass filter. Combining Eqs. (1) and (2), we find

$$\begin{aligned}\overline{r}(\mathbf{x})&=\frac{1}{2\pi z_0}\int_{-\infty}^{\infty}d\mathbf{x}'\tilde{h}(\mathbf{x}-\mathbf{x}')\frac{\partial^2 z(\mathbf{x}')}{\partial x_1'^2}\\&=[h\otimes z](\mathbf{x}),\quad \text{where } h(\mathbf{x})\triangleq\frac{1}{2\pi z_0}\frac{\partial^2\tilde{h}(\mathbf{x})}{\partial x_1^2}.\end{aligned} \tag{3}$$

The symbol $\otimes$ denotes 1-D, 2-D, or 3-D convolution depending on the dimension of $\mathbf{x}$. While h is deterministic, z is an ergodic, zero-mean, Gaussian random process.

The final form of Eq. (3) was introduced to strain imaging by Bertrand and colleagues[27,40] to relate the echo signal directly to the impedance distribution. Therein, signals from a deformed scattering medium can be written in terms of the object function $z(\mathbf{x})$ through a coordinate transformation on $\mathbf{x}$. The quantity h is the sensitivity function. It includes the point-spread function of the ultrasound system, but, more precisely, it is the mapping between the object function z and the echo signal $\overline{r}$. Notice that for an ideal imaging system where $\tilde{h}(\mathbf{x})=\delta(\mathbf{x})$, the Dirac delta function, then

$$\overline{r}(\mathbf{x})=\frac{1}{2\pi z_0}\frac{\partial^2 z(\mathbf{x}')}{\partial x_1'^2}\bigg|_{\mathbf{x}'=\mathbf{x}}.$$

B. Object deformation and coordinate transformation

Strain is estimated through a process that correlates ultrasonic waveform segments recorded before and after a static stress field is applied to the medium being imaged. To be able to evaluate strain estimators, we need a model of the ultrasonic waveform that is both accurate and mathematically tractable. An essential component of such a model is the ability to express coordinates of the impedance distribution before deformation, labeled $\tilde{\mathbf{x}}$, in terms of those after deformation, $\mathbf{x}$, viz., $z(\tilde{\mathbf{x}}(\mathbf{x},t_j))$ where

$$\tilde{\mathbf{x}}(\mathbf{x},t_j)=(\tilde{x}_1(x_1,x_2,x_3,t_j),\tilde{x}_2(x_1,x_2,x_3,t_j),$$
$$\tilde{x}_3(x_1,x_2,x_3,t_j))^t,$$

$j=0,1,2,...$, and $\tilde{\mathbf{x}}(\mathbf{x},t_0)=\mathbf{x}$. The time variable denotes the waveform field recorded during the jth compression at time t_j. In this analysis single-compression strain images are studied: t_0 indicates the time of recording for the precompression waveform field and t_1 is the time of recording following the first compression. However, the analysis is easily extended to multicompression techniques. The corresponding waveforms, expressed in the post-compression coordinates $\mathbf{x}$, at each t_j are given by

$$r(\mathbf{x},t_j)=\overline{r_j}(\mathbf{x})+n_j(\mathbf{x})$$
$$=\left[\int_{\mathcal{S}} d\mathbf{x}'\,h(\mathbf{x}-\mathbf{x}')z(\tilde{\mathbf{x}}(\mathbf{x}',t_j))\right]+n_j(\mathbf{x}), \qquad (4)$$

where $\mathcal{S}$ is the region of support as discussed below and defined as usual.[41] Noise processes $n_j(\mathbf{x})$ are signal independent, zero-mean, bandpass white, and Gaussian with power spectral density G_n, i.e.,

$$E\{n^*(\mathbf{x})z(\mathbf{x})\}=0, \quad E\{n(\mathbf{x})\}=0,$$
$$E\{n^*(\mathbf{x})n(\mathbf{x}')\}=G_n\delta(\mathbf{x}-\mathbf{x}'),$$

where n^* is the complex conjugate of n and $E\{\cdots\}$ denotes expectation.[42]

At time t_0, Eq. (4) reduces to $r(\mathbf{x},t_0)=[h\otimes z](\mathbf{x})+n_0(\mathbf{x})$, the pre-compression echo waveform. At t_1, the post-compression acoustic impedance field is described by $z(\tilde{\mathbf{x}}(\mathbf{x},t_1))$ that explicitly relates the pre-compression position of the impedance field $\tilde{\mathbf{x}}$ to the post-compression position $\mathbf{x}$. We refer to the set of radio-frequency (rf) waveforms in a scan plane acquired at frame time t_j as an *echo field*.

An affine mapping between $\tilde{\mathbf{x}}$ and $\mathbf{x}$ is defined by the linear transformation matrix $\mathbf{A}$, the translation vector $\boldsymbol{\tau}_a$, and the equations

$$\begin{aligned}\mathbf{x}(\tilde{\mathbf{x}},t_j)&=\mathbf{A}\tilde{\mathbf{x}}+\mathbf{A}\boldsymbol{\tau}_a\\ \tilde{\mathbf{x}}(\mathbf{x},t_j)&=\mathbf{A}^{-1}\mathbf{x}-\boldsymbol{\tau}_a\end{aligned} \quad \text{for } j\geqslant 0, \qquad (5)$$

where

$$\mathbf{A}=\left(\begin{array}{ccc}\frac{\partial x_1}{\partial\tilde{x}_1} & \frac{\partial x_1}{\partial\tilde{x}_2} & \frac{\partial x_1}{\partial\tilde{x}_3}\\ \frac{\partial x_2}{\partial\tilde{x}_1} & \frac{\partial x_2}{\partial\tilde{x}_2} & \frac{\partial x_2}{\partial\tilde{x}_3}\\ \frac{\partial x_3}{\partial\tilde{x}_1} & \frac{\partial x_3}{\partial\tilde{x}_2} & \frac{\partial x_3}{\partial\tilde{x}_3}\end{array}\right)_{(\mathbf{0},t_j)}, \quad \boldsymbol{\tau}_a=\left(\begin{array}{c}\tau_{a,1}\\ \tau_{a,2}\\ \tau_{a,3}\end{array}\right)_{t_j}. \qquad (6)$$

$\mathbf{A}$ and $\boldsymbol{\tau}_a$ are implicit functions of t_j since the transformation at any $\tilde{\mathbf{x}}$ varies for each level of compression; e.g., at $j=0$, $\boldsymbol{\tau}_a=\mathbf{0}$, and $\mathbf{A}=\mathbf{I}$, the identity matrix. Another example is the deformation of a homogeneous and incompressible (Poisson's ratio $\simeq 0.5$) medium, where the object is uniformly squeezed by a small amount along the x_1-axis. In this case, the deformation may be described as a scaling of the echo coordinates, and $\mathbf{A}$ is diagonal with nonzero elements $A_{11}=1-s$, $A_{22}=A_{33}=1/\sqrt{1-s}\simeq 1+s/2$. If Eqs. (5) and (6) are to accurately represent the effects of strain s, two conditions must be satisfied: the mapping from $\tilde{\mathbf{x}}$ to $\mathbf{x}$ must be linear over $\mathcal{S}$, and the components of the transformation matrix must be linear functions of strain as in the example above. Both conditions are satisfied if the applied deformations are small.

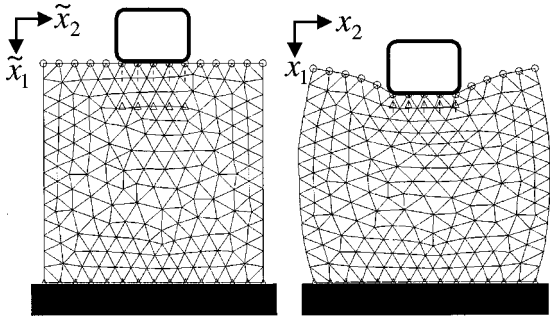

FIG. 1. Deformation of an elastically uniform medium.

Many biological tissues are linear-elastic and incompressible for small deformations.[24] Shear modulus is the material property that describes the deformation of an incremental volume into an equal volume of altered shape. A volume cannot be transformed into a plane, a line, or a point by this operation, so the matrix $\mathbf{A}$ must have rank 3. The mapping from one space to the other is one to one, the inverse $\mathbf{A}^{-1}$ exists, and the Jacobian of the forward transformation, which is the determinant of $\mathbf{A}$, $\det\mathbf{A}$, is nonzero. Furthermore, for incompressible media, $\det\mathbf{A}=1$, which means the volume is conserved. Equation (5) is critical for describing how physical deformation of the object affects coherence between the pre- and post-compression waveforms. In our experience with tissuelike media, deformations are often spatially smooth, particularly over the dimensions of the ultrasonic pulse volume. So the first line of Eq. (5) may be considered a first-order Maclaurin series expansion of $\mathbf{x}(\tilde{\mathbf{x}},t_j)$. It is an accurate approximation of $\mathbf{x}$ in a neighborhood of $\tilde{\mathbf{x}}=\mathbf{0}$. The deformation of a large object region in a strain image may be described by segmenting echo fields into neighborhoods and determining the first-order Maclaurin series for each (Fig. 1).

C. Waveform warping

Our original deformation model was limited to scaling.[43] Large displacement errors were found when using correlation techniques if either of the signals to be cross correlated were scaled relative to the other. To minimize the effects of scaling deformation on displacement estimation, waveforms were compressed and expanded—companded—in one,[30,43] two,[26] or three[44] dimensions prior to correlation. The purpose was to eliminate the scaling component of deformation over the dimensions of the correlation data kernel size and larger. Companding significantly reduces strain noise whenever scaling is the principal deformation.

For more general types of motion, we *warp* the pre-compression echo field prior to cross correlation.[29] Warping may be achieved by applying the transformation $\mathbf{x}(\tilde{\mathbf{x}},t_0)=\mathbf{B}\tilde{\mathbf{x}}+\mathbf{B}\boldsymbol{\tau}_b$ to $r(\tilde{\mathbf{x}},t_0)$ to find $r(\mathbf{B}^{-1}\mathbf{x}-\boldsymbol{\tau}_b,t_0)$. The criterion for selecting $\mathbf{B}$ and $\boldsymbol{\tau}_b$ is that they maximize the magnitude squared coherence function defined in Eq. (12) below. Using the notation of Eq. (5) and the post-compression coordinates

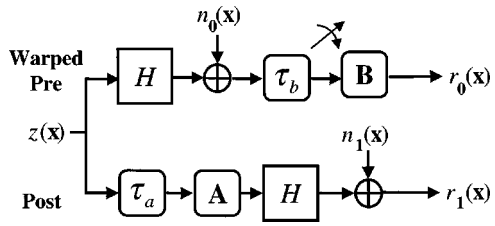

FIG. 2. Ultrasonic waveform model of Eq. (7).

x, the waveforms for single-compression static strain imaging using pulse-echo ultrasound signals, Eq. (4), may be written as

$$
\begin{aligned}
r(\mathbf{x},t_0) &= [h\otimes z](\mathbf{x}) + n_0(\mathbf{x}), && \text{Pre}\\
r_0(\mathbf{x}) &\triangleq r(\mathbf{B}^{-1}\mathbf{x}-\boldsymbol{\tau}_b, t_0),\\
&= \left[\int_{\mathcal{S}} d\mathbf{x}' h(\mathbf{B}^{-1}\mathbf{x}-\boldsymbol{\tau}_b-\mathbf{x}')z(\mathbf{x}')\right]\\
&\quad + n_0(\mathbf{B}^{-1}\mathbf{x}-\boldsymbol{\tau}_b), && \text{Warped Pre}\\
&= \overline{r}_0(\mathbf{x}) + n_0(\mathbf{B}^{-1}\mathbf{x}-\boldsymbol{\tau}_b), && (7)\\
r_1(\mathbf{x}) &\triangleq r(\mathbf{x},t_1)\\
&= \left[\int_{\mathcal{S}} d\mathbf{x}' h(\mathbf{x}-\mathbf{x}')z(\mathbf{A}^{-1}\mathbf{x}'-\boldsymbol{\tau}_a)\right] + n_1(\mathbf{x}), && \text{Post}\\
&= \overline{r}_1(\mathbf{x}) + n_1(\mathbf{x}).
\end{aligned}
$$

Matrix **A** is a linear transformation that describes the physical deformation of the impedance field from a force applied to the object, and **B** is the linear transformation that describes the warp applied to the precompression echo field through signal processing. Eq. (7) is illustrated in Fig. 2.

Warping cannot fully restore lost coherence even for noise-free waveforms. First, the sensitivity function h introduces a null space[45] in which small-scale object deformations cannot be observed using echo waveforms. Consequently, echo formation and object deformation are not commutative operations (Fig. 2). Second, a typical strain image is generated from a plane of echo data. While **A** is given by Eq. (6), **B** has the form

$$
\mathbf{B} = \begin{pmatrix} \dfrac{\partial x_1}{\partial \tilde{x}_1} & \dfrac{\partial x_1}{\partial \tilde{x}_2} & 0\\ \dfrac{\partial x_2}{\partial \tilde{x}_1} & \dfrac{\partial x_2}{\partial \tilde{x}_2} & 0\\ 0 & 0 & 1 \end{pmatrix}, \quad \boldsymbol{\tau}_b = \begin{pmatrix} \tau_{b,1}\\ \tau_{b,2}\\ 0 \end{pmatrix}. \tag{8}
$$

Here too is a null space that reduces coherence in a manner that cannot be recovered by signal processing. The first cause for coherence loss is minimized using highly focused, high bandwidth ultrasound pulses. The second cause is minimized by finely sampling data from a volume instead of a plane or restricting all motion to the scan plane. Nevertheless, we show below that filtering and cross correlating r_0 and r_1 is the maximum-likelihood strategy for estimating displacement. Equation (7) extends our previous 1-D waveform model[46] to three dimensions.

D. Definitions

A few important quantities and relations well known from the literature are stated below without proof and in the notation of this paper.

We assume 2-D echo fields, $r_j(\mathbf{x})$, $j=0,1$, are acquired from the object in a rectangular region defined by the set $\mathcal{S}$ of measure $\mathcal{S}'$.[41] The Fourier series coefficient estimates $\hat{R}_{jk}$ of the 2-D echo field are[47]

$$
\hat{R}_{jk} = \frac{1}{\mathcal{S}'}\int_{\mathcal{S}} d\mathbf{x} r_j(\mathbf{x}) e^{-i2\pi \mathbf{u}_k^t \mathbf{x}}. \tag{9}
$$

Wave vectors $\mathbf{u}_k$ define points on an infinite 2-D grid.[48] For convenience, the two integer indices required to define the grid are lumped into a single index $k=1,\ldots,N$ that enumerates all N frequency points within $\mathcal{S}$.[49] $\hat{R}_{jk}$ is a complex, Gaussian random process because the real waveform $r_j(\mathbf{x})$ is Gaussian.

The Fourier transform of $r_j(\mathbf{x})$ is[47]

$$
R_j(\mathbf{u}) = \lim_{\mathcal{S}'\to\infty} \mathcal{S}'\hat{R}_{jk} = \int_{-\infty}^{\infty} d\mathbf{x} r_j(\mathbf{x}) e^{-i2\pi \mathbf{u}^t \mathbf{x}}, \tag{10}
$$

where **u** is a continuous 2-D spatial frequency variable. It has been shown[50,51] that if the dimensions of the support function are large compared to those of the correlation area in r_j plus the translation $\boldsymbol{\tau}_a$, then the cross power spectral density is

$$
\begin{aligned}
G_{r_0 r_1}(\mathbf{u}_k) &= \mathcal{S}'^2 E\{\hat{R}_{0k}^* \hat{R}_{1k'}\} \xrightarrow[\mathcal{S}',N\to\infty]{} G_{r_0 r_1}(\mathbf{u})\\
&= E\{R_0^*(\mathbf{u}) R_1(\mathbf{u})\}. \qquad (11)
\end{aligned}
$$

If $G_{r_0 r_0}(\mathbf{u})$ and $G_{r_1 r_1}(\mathbf{u})$ are the autospectral densities, then the complex coherence and magnitude squared coherence (MSC) functions are, respectively,

$$
\begin{aligned}
\gamma_{r_0 r_1}(\mathbf{u}) &\triangleq \frac{G_{r_0 r_1}(\mathbf{u})}{\sqrt{G_{r_0 r_0}(\mathbf{u}) G_{r_1 r_1}(\mathbf{u})}},\\
|\gamma_{r_0 r_1}(\mathbf{u})|^2 &= \frac{|G_{r_0 r_1}(\mathbf{u})|^2}{G_{r_0 r_0}(\mathbf{u}) G_{r_1 r_1}(\mathbf{u})},
\end{aligned} \tag{12}
$$

where $0 \leqslant |\gamma_{r_0 r_1}(\mathbf{u})|^2 \leqslant 1$.[52]

Finally, the Fourier transform of a single realization of a scalar random function whose vector coordinates undergo a linear transformation and translation is given by

$$
\mathcal{F}\{z(\mathbf{A}^{-1}\mathbf{x}-\boldsymbol{\tau}_a)\} = \det \mathbf{A} Z(\mathbf{A}^t \mathbf{u}) e^{-i2\pi \mathbf{u}^t \mathbf{A} \boldsymbol{\tau}_a}. \tag{13}
$$

Related results are derived in Appendix A and in Ref. 27.

II. POWER SPECTRAL DENSITY AND COHERENCE

The goal of this section is to express power spectral density functions of the pre- and post-compression waveforms in terms of the signal model of Eq. (7).

A. Cross-spectral density

Assume two-dimensional echo fields are recorded using a linear array transducer. For a rectangular support region $\mathcal{S}$ with dimensions $\mathcal{S}'=T_1T_2$,[41] we find from Eqs. (9) and (11) that

$$E\{\hat{R}_{0k}^{*}\hat{R}_{1k'}\}=\frac{1}{\mathcal{S}'^2}\int_{\mathcal{S}}d\mathbf{x}\int_{\mathcal{S}}d\mathbf{x}'\,\phi_{r_0r_1}(\mathbf{x},\mathbf{x}')\times e^{i2\pi(\mathbf{u}_k^t\mathbf{x}-\mathbf{u}_{k'}^t\mathbf{x}')}. \tag{14}$$

Using Eqs. (45) and (47) from Appendix A and the Wiener–Kinchin theorem,[53] the mean cross correlation function for the echo waveforms is[25]

$$\begin{aligned}\phi_{r_0r_1}(\mathbf{x},\mathbf{x}')&\triangleq E\{r_0^{*}(\mathbf{x})r_1(\mathbf{x}')\}\\&=\det\mathbf{A}\det\mathbf{B}\int_{-\infty}^{\infty}d\boldsymbol{\xi}H(\boldsymbol{\xi})H^{*}(\mathbf{B}^t\boldsymbol{\xi})\\&\quad\times E\{Z(\mathbf{A}^t\boldsymbol{\xi})Z^{*}(\mathbf{B}^t\boldsymbol{\xi})\}\\&\quad\times e^{i2\pi\boldsymbol{\xi}^t(\mathbf{x}'-\mathbf{x}-\mathbf{A}\boldsymbol{\tau}_a+\mathbf{B}\boldsymbol{\tau}_b)}.\end{aligned} \tag{15}$$

Notice that r_0 and r_1 are individually stationary processes but jointly nonstationary. Equations (14) and (15) may be extended to three dimensions to track motion within a scan-volume data set.[44]

Combining Eqs. (14) and (15) and integrating with respect to $\mathbf{x}$ and $\mathbf{x}'$ we find

$$\begin{aligned}E\{\hat{R}_{0k}^{*}\hat{R}_{1k'}\}&=\frac{\det\mathbf{A}\det\mathbf{B}}{\mathcal{S}'}\int_{-\infty}^{\infty}d\boldsymbol{\xi}H(\boldsymbol{\xi})H^{*}(\mathbf{B}^t\boldsymbol{\xi})\\&\quad\times E\{Z(\mathbf{A}^t\boldsymbol{\xi})Z^{*}(\mathbf{B}^t\boldsymbol{\xi})\}e^{-i2\pi\boldsymbol{\xi}^t(\mathbf{A}\boldsymbol{\tau}_a-\mathbf{B}\boldsymbol{\tau}_b)}\\&\quad\times T_1\frac{\sin\pi(\xi_1-u_{1k})T_1}{\pi(\xi_1-u_{1k})T_1}\frac{\sin\pi(\xi_1-u_{1k'})T_1}{\pi(\xi_1-u_{1k'})T_1}\\&\quad\times T_2\frac{\sin\pi(\xi_2-u_{2k})T_2}{\pi(\xi_2-u_{2k})T_2}\frac{\sin\pi(\xi_2-u_{2k'})T_2}{\pi(\xi_2-u_{2k'})T_2}.\end{aligned} \tag{16}$$

Increasing T_1 and T_2 while holding $\mathbf{u}_k$ and $\mathbf{u}_{k'}$ constant yields[54]

$$E\{\hat{R}_{0k}^{*}\hat{R}_{1k'}\}\simeq\begin{cases}\dfrac{\det\mathbf{A}\det\mathbf{B}}{\mathcal{S}'}H(\mathbf{u}_k)H^{*}(\mathbf{B}^t\mathbf{u}_k)E\{Z(\mathbf{A}^t\mathbf{u}_k)Z^{*}(\mathbf{B}^t\mathbf{u}_k)\}e^{-i2\pi\mathbf{u}_k^t(\mathbf{A}\boldsymbol{\tau}_a-\mathbf{B}\boldsymbol{\tau}_b)} & \text{for } k'=k\\ 0 \quad \text{for } k'\neq k\end{cases}. \tag{17}$$

Selection of harmonic frequencies, e.g., $u_{1k}=k/T_1$, is sufficient to ensure that frequency components of the cross-spectral density are orthogonal. The approximation in Eq. (17) approaches an equality as (a) $\mathcal{S}'$ becomes large or the other factors in the integrand do not vary over the frequency interval and (b) the displacement becomes small, specifically, $\tau_{a1}\ll T_1$. Weighting the data with an apodized window function correlates frequency components and can interfere with the orthogonality that must be achieved if data warping followed by cross correlation is to be a maximum-likelihood estimator, as discussed below. The orthogonality condition depends only on properties of the measurement and not the object.

B. Autospectral density

Following the above development, and combining Eqs. (11), (A3), and (A5) yields

$$E\{\hat{R}_{0k}^{*}\hat{R}_{0k'}\}=\begin{cases}\dfrac{(\det\mathbf{B})^2}{\mathcal{S}'}(|H(\mathbf{B}^t\mathbf{u}_k)|^2E\{|Z(\mathbf{B}^t\mathbf{u}_k)|^2\}\\ \quad+E\{|\hat{N}_{0Bk}|^2\}) \quad \text{for } k'=k\\ 0 \quad \text{for } k'\neq k\end{cases},$$

$$E\{\hat{R}_{1k}^{*}\hat{R}_{1k'}\}=\begin{cases}\dfrac{1}{\mathcal{S}'}((\det\mathbf{A})^2|H(\mathbf{u}_k)|^2E\{|Z(\mathbf{A}^t\mathbf{u}_k)|^2\}\\ \quad+E\{|\hat{N}_{1k}|^2\}) \quad \text{for } k'=k\\ 0 \quad \text{for } k'\neq k\end{cases}. \tag{18}$$

For white noise, $E\{|\hat{N}_{0Bk}|^2\}=E\{|\hat{N}_{1k}|^2\}=G_n/\mathcal{S}'^2$. Equations (17) and (18) show that the spectral density functions of the pre- and post-compression echo fields depend on the pulse-echo transfer function of the ultrasonic imaging system via H, the physical deformation via $\mathbf{A}$ and $\boldsymbol{\tau}_a$, and the applied warp via $\mathbf{B}$ and $\boldsymbol{\tau}_b$.

C. Complex coherence

The next section will show the importance of the MSC function for modeling the performance of strain imaging. An expression for MSC is found by substituting Eqs. (17) and (18) into Eq. (12). For a continuous frequency variable, we find

$$|\gamma_{r_0r_1}(\mathbf{u})|^2=\frac{|\gamma_{z_0z_1}(\mathbf{u})|^2\mathrm{SNR}(\mathbf{u})}{1+\mathrm{SNR}(\mathbf{u})}, \tag{19}$$

where

$$|\gamma_{z_0z_1}(\mathbf{u})|^2=\frac{E\{Z(\mathbf{A}^t\mathbf{u})Z^{*}(\mathbf{B}^t\mathbf{u})\}E\{Z^{*}(\mathbf{A}^t\mathbf{u})Z(\mathbf{B}^t\mathbf{u})\}}{E\{|Z(\mathbf{A}^t\mathbf{u})|^2\}E\{|Z(\mathbf{B}^t\mathbf{u})|^2\}} \tag{20}$$

is the MSC for the object function,

$$\mathrm{SNR}(\mathbf{u})\triangleq\frac{S/N_0(\mathbf{u})S/N_1(\mathbf{u})}{1+S/N_0(\mathbf{u})+S/N_1(\mathbf{u})} \tag{21}$$

is the net signal-to-noise ratio,[55] and

$$S/N_0(\mathbf{u}) = \frac{|H(\mathbf{B}^t\mathbf{u})|^2 E\{|Z(\mathbf{B}^t\mathbf{u})|^2\}}{E\{|N_0(\mathbf{B}^t\mathbf{u})|^2\}},$$
$$S/N_1(\mathbf{u}) = \frac{(\det\mathbf{A})^2|H(\mathbf{u})|^2 E\{|Z(\mathbf{A}^t\mathbf{u})|^2\}}{E\{|N_1(\mathbf{u})|^2\}} \tag{22}$$

are channel signal-to-noise ratios corresponding to the warped pre- and post-compression echo waveforms, respectively. The echo waveform MSC is the frequency-space analog to the correlation coefficient. It depends on the object function MSC and SNR($\mathbf{u}$) that includes properties of the imaging system, scattering medium, and noise.

MSC defines the similarity between r_0 and r_1. Intuition tells us that it will be easier to measure displacement if r_0 is similar to r_1, e.g., rigid-body displacement. More intuition about Eq. (19) is found through examples. First, in a simple ideal case, the channel signal-to-noise ratios are large at all frequencies in the bandwidth, $S/N_0 \simeq S/N_1 \gg 1$, and we compress the object a small amount ($<1\%$ of its size) and warp the waveforms accordingly; $\mathbf{A}=\mathbf{B}\simeq\mathbf{I}$. Then SNR($\mathbf{u}$) $\simeq 0.5 S/N_j$ and $|\gamma_{r_0r_1}(\mathbf{u})|^2 \simeq 1$. Low-compression strain images are contrast limited. In a second, more complicated ideal situation, we physically deform the object a substantial amount, say 5% to 10%, to ensure ample strain contrast. Then we apply the perfect warp, i.e., $\mathbf{B}=\mathbf{A}$. In this case, $|\gamma_{z_0z_1}|^2 \simeq 1$ and yet $|\gamma_{r_0r_1}|^2 < 1$ because $S/N_0 \neq S/N_1$ unless all scatterers are resolved by the ultrasonic imaging system such that $|H(\mathbf{B}^t\mathbf{u})|^2 \simeq |H(\mathbf{u})|^2$ over all frequencies for which $|Z(\mathbf{u})|^2$ is nonzero. Unfortunately the bandwidth of the object response is usually much broader than that of the imaging system, and the resulting null space leads to a loss of coherence even for a perfect warp. High-compression strain images are noise limited. Third, if the warp does not match the physical deformation, $\mathbf{B}\neq\mathbf{A}$, then coherence is lost regardless of SNR($\mathbf{u}$) because $|\gamma_{z_0z_1}|^2 < 1$. Ultrasonic attenuation reduces coherence only at frequencies where $S/N_j \not\gg 1$. We show in the next section that accurate displacement estimates require that we design the experiment and image formation algorithm to achieve MSC close to one.

III. MAXIMUM-LIKELIHOOD DISPLACEMENT ESTIMATION

The maximum-likelihood (ML) estimator for displacement selects the estimate $\hat{\boldsymbol{\tau}}$ that maximizes the value of the likelihood function $p(\hat{\mathbf{R}}|\boldsymbol{\theta})$,[56,57] or a monotonic transformation of $p(\hat{\mathbf{R}}|\boldsymbol{\theta})$. $\boldsymbol{\theta}$ is a vector of all unknown real parameters that affect the data, viz., the elements of $\mathbf{A}$, $\mathbf{B}$, $\boldsymbol{\tau}_a$, $\boldsymbol{\tau}_b$, $|H_k|^2$, $E\{|\hat{Z}_{jk}|^2\}$, and $E\{|\hat{N}_{jk}|^2\}$. It is convenient to define the complete data vector $\hat{\mathbf{R}}=(\hat{R}_{01},\hat{R}_{11},\ldots\hat{R}_{0k},\hat{R}_{1k},\ldots\hat{R}_{0N},\hat{R}_{1N})^t$ of length $2N$. It interlaces Fourier-series coefficient pairs from the warped pre- and post-compression echo fields over all N frequencies.[51] Since each value of $\hat{R}_{0k}$ and $\hat{R}_{1k}$ is a complex, Gaussian random variable, the likelihood function is multivariate, complex, and Gaussian in $2N$ dimensions:

$$p(\hat{\mathbf{R}}|\boldsymbol{\theta}) = \frac{\mathcal{S}'^{4N}}{(2\pi)^{2N}\det(\mathbf{Q})}\exp\left(-\frac{\mathcal{S}'^2}{2}\hat{\mathbf{R}}^\dagger\mathbf{Q}^{-1}\hat{\mathbf{R}}\right), \tag{23}$$

where $\hat{\mathbf{R}}^\dagger$ is the complex conjugate transpose (adjoint) of $\hat{\mathbf{R}}$, $E\{\hat{\mathbf{R}}\}=\mathbf{0}$, and

$$\mathbf{Q} \triangleq \mathcal{S}'^2 E\{\hat{\mathbf{R}}\hat{\mathbf{R}}^\dagger\}$$

is a spectral density matrix. The effects on $\hat{\mathbf{R}}$ of object deformation, translation, rotation, and data warping are completely specified by $\mathbf{Q}$.

The $2N\times 2N$ Hermitian matrix $\mathbf{Q}$ may be thought of as an $N\times N$ block-diagonal matrix of 2×2 Hermitian submatrices $\mathbf{Q}_{kk'}$. Since the frequency components are orthogonal, $\mathbf{Q}_{kk'}=\mathbf{Q}_k\delta_{kk'}$, where $\delta_{kk'}$ is the Kroneker delta function, and[50]

$$\mathbf{Q}_k = \begin{pmatrix} G_{r_0r_0}(\mathbf{u}_k) & G^*_{r_0r_1}(\mathbf{u}_k) \\ G_{r_0r_1}(\mathbf{u}_k) & G_{r_1r_1}(\mathbf{u}_k) \end{pmatrix}. \tag{24}$$

Each of the N submatricies $\mathbf{Q}_k=\mathcal{S}'^2E\{\hat{\mathbf{R}}_k\hat{\mathbf{R}}_k^\dagger\}$, where $\hat{\mathbf{R}}_k=(\hat{R}_{0k},\hat{R}_{1k})$, are statistically independent. Also,

$$\det\mathbf{Q}_k = G_{r_0r_0}(\mathbf{u}_k)G_{r_1r_1}(\mathbf{u}_k)(1-|\gamma_{r_0r_1}(\mathbf{u}_k)|^2)$$

and

$$\mathbf{Q}_k^{-1} = \begin{pmatrix} \frac{1}{G_{r_0r_0}(\mathbf{u}_k)} & \frac{-\gamma^*_{r_0r_1}(\mathbf{u}_k)}{\sqrt{G_{r_0r_0}(\mathbf{u}_k)G_{r_1r_1}(\mathbf{u}_k)}} \\ \frac{-\gamma_{r_0r_1}(\mathbf{u}_k)}{\sqrt{G_{r_0r_0}(\mathbf{u}_k)G_{r_1r_1}(\mathbf{u}_k)}} & \frac{1}{G_{r_1r_1}(\mathbf{u}_k)} \end{pmatrix} \times(1-|\gamma_{r_0r_1}(\mathbf{u}_k)|^2)^{-1}. \tag{25}$$

In practice, waveforms always contain noise, so $(1-|\gamma_{r_0r_1}(\mathbf{u}_k)|^2)>0$ and $\mathbf{Q}_k^{-1}$ exists.

The logarithm of the likelihood function is

$$\ln p(\hat{\mathbf{R}}|\boldsymbol{\theta}) = 4N\ln\mathcal{S}' - 2N\ln 2\pi - \ln\det\mathbf{Q} - \frac{\mathcal{S}'^2}{2}\hat{\mathbf{R}}^\dagger\mathbf{Q}^{-1}\hat{\mathbf{R}}. \tag{26}$$

The first three terms of Eq. (26) can be ignored since they are independent of τ_a and weakly dependent on $\mathbf{A}$. Expanding the last term, we find

$$\ln p(\hat{\mathbf{R}}|\boldsymbol{\theta}) \simeq -\frac{\mathcal{S}'^2}{2}\sum_{k=1}^{N}\frac{1}{1-|\gamma_{r_0r_1}(\mathbf{u}_k)|^2}\left[\frac{|\hat{R}_{0k}|^2}{G_{r_0r_0}(\mathbf{u}_k)} + \frac{|\hat{R}_{1k}|^2}{G_{r_1r_1}(\mathbf{u}_k)} - \frac{\hat{R}^*_{0k}\hat{R}_{1k}\gamma^*_{r_0r_1}(\mathbf{u}_k)}{\sqrt{G_{r_0r_0}(\mathbf{u}_k)G_{r_1r_1}(\mathbf{u}_k)}} - \frac{\hat{R}_{0k}\hat{R}^*_{1k}\gamma_{r_0r_1}(\mathbf{u}_k)}{\sqrt{G_{r_0r_0}(\mathbf{u}_k)G_{r_1r_1}(\mathbf{u}_k)}}\right]. \tag{27}$$

Again, the first two terms in the square brackets are weakly dependent on the motion parameters and therefore can be safely ignored for our purposes. The remaining two terms may be written as

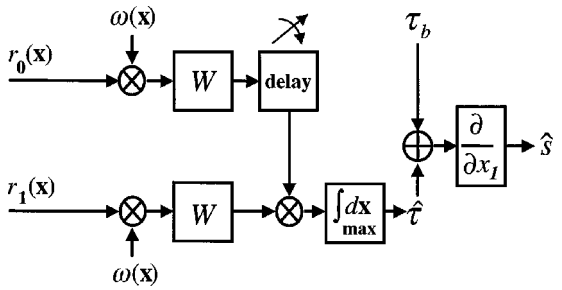

FIG. 3. Generalized cross correlator and strain estimator. The quantity $\omega(\mathbf{x})$ is a window function.

$$\ln p(\hat{\mathbf{R}}|\boldsymbol{\theta}) \simeq \mathcal{S}'^2 \sum_{k=1}^{N} \mathrm{Re}\{\hat{R}_{0k}^* \hat{R}_{1k} W^2(\mathbf{u}_k) \times e^{-i2\pi \mathbf{u}_k^t (\mathbf{A}\boldsymbol{\tau}_a - \mathbf{B}\boldsymbol{\tau}_b)}\}, \tag{28}$$

where $\mathrm{Re}\{\cdots\}$ is the real part of the argument and

$$W^2(\mathbf{u}_k) = \frac{|\gamma_{r_0 r_1}(\mathbf{u}_k)|}{\sqrt{G_{r_0 r_0}(\mathbf{u}_k) G_{r_1 r_1}(\mathbf{u}_k)}(1-|\gamma_{r_0 r_1}(\mathbf{u}_k)|^2)}$$

is a real function of frequency. For large $\mathcal{S}'$, Eq. (11) can be used to express the log-likelihood function of Eq. (28) as an integral over a continuous frequency variable,

$$\ln p(\hat{\mathbf{R}}|\boldsymbol{\theta}) \simeq \mathcal{S}' \int_{-\infty}^{\infty} d\mathbf{u}\, \mathrm{Re}\{R_0^*(\mathbf{u}) R_1(\mathbf{u}) W^2(\mathbf{u}) \times e^{-i2\pi \mathbf{u}^t (\mathbf{A}\boldsymbol{\tau}_a - \mathbf{B}\boldsymbol{\tau}_b)}\}. \tag{29}$$

The first factor in the braces of Eq. (29), $R_0^*(\mathbf{u}) R_1(\mathbf{u})$, is the frequency-space representation of the cross correlation between echo waveforms *for a specific data kernel*. The second factor, $W^2(\mathbf{u})$, is a filter function that weights the Fourier coefficients of the data based on coherence. The third (phase) factor is a function of the physical displacement $\mathbf{A}\boldsymbol{\tau}_a$ and warp displacement $\mathbf{B}\boldsymbol{\tau}_b$. If we write

$$R_0^*(\mathbf{u}) R_1(\mathbf{u}) = \hat{G}_{r_0 r_1}(\mathbf{u}) = |\hat{\gamma}_{r_0 r_1}(\mathbf{u})| e^{i2\pi \mathbf{u}^t \hat{\boldsymbol{\tau}}} \sqrt{G_{r_0 r_0}(\mathbf{u}) G_{r_1 r_1}(\mathbf{u})}, \tag{30}$$

where $G_{r_0 r_1}(\mathbf{u}) = E\{\hat{G}_{r_0 r_1}(\mathbf{u})\}$, then

$$\ln p(\hat{\mathbf{R}}|\boldsymbol{\theta}) \simeq \mathcal{S}' \int_{-\infty}^{\infty} d\mathbf{u} \frac{|\hat{\gamma}_{r_0 r_1}(\mathbf{u})||\gamma_{r_0 r_1}(\mathbf{u})|}{(1-|\gamma_{r_0 r_1}(\mathbf{u})|^2)} \times \mathrm{Re}\{e^{-i2\pi \mathbf{u}^t (\mathbf{A}\boldsymbol{\tau}_a - \mathbf{B}\boldsymbol{\tau}_b - \hat{\boldsymbol{\tau}})}\}. \tag{31}$$

ML estimates of displacement are those that satisfy $\partial \ln p(\hat{\mathbf{R}}|\boldsymbol{\theta})/\partial \hat{\boldsymbol{\tau}} = \mathbf{0}$. Equation (29) is one way to view the ML strategy: (a) Warp the echo fields in a way that maximizes the coherence between r_0 and r_1 (Fig. 2). (b) Increase the relative weighting of frequency components with the highest coherence using W. (c) Cross correlate r_0 and r_1 to find $\hat{\boldsymbol{\tau}}$ at the peak value and add to $\mathbf{B}\boldsymbol{\tau}_b$. Hence, the ML strategy for displacement estimation in acoustic strain imaging (Fig. 3) is consistent with the generalized cross correlator approach described by Knapp and Carter if it is extended to higher spatial dimensions.[25,50] Maximizing waveform coherence also maximizes the peak of the cross correlation function.

The phase factor in Eq. (31) is unity at all frequencies only when the estimate is accurate: $\hat{\boldsymbol{\tau}} + \mathbf{B}\boldsymbol{\tau}_b = \mathbf{A}\boldsymbol{\tau}_a$. Otherwise, motion along all three axes affects displacement estimates along each axis, and the integrand becomes an oscillating function of frequency with decreasing envelope. The oscillations, which are about zero, increase in frequency as $\mathbf{A}\boldsymbol{\tau}_a - \mathbf{B}\boldsymbol{\tau}_b - \hat{\boldsymbol{\tau}}$ deviates further from zero, dramatically reducing the value of the log-likelihood function. The mean log-likelihood function is maximum when $E\{\hat{\boldsymbol{\tau}}\} = \mathbf{A}\boldsymbol{\tau}_a - \mathbf{B}\boldsymbol{\tau}_b = \mathbf{0}$, $\mathbf{A} = \mathbf{B} \simeq \mathbf{I}$, and $\boldsymbol{\tau}_a = \boldsymbol{\tau}_b$, which is also a situation that provides uninteresting strain images. The challenge for medical imaging applications is to achieve maximum-likelihood estimation for displacement in less optimal but more interesting situations.

A. Relationships

The log-likelihood function of Eq. (29) is related to important estimation criteria found in the literature. By beginning the derivation with Fourier coefficients of the data, Eq. (29) becomes the characteristic function of l_r, the classical log-likelihood function defined by Van Trees for zero-mean random signals:[31]

$$\begin{aligned} l_r(\boldsymbol{\theta}) &= \mathcal{F}^{-1}\{\ln p(\hat{\mathbf{R}}|\boldsymbol{\theta})\} \\ &= C \int_{-\infty}^{\infty} d\mathbf{y} \int_{-\infty}^{\infty} d\mathbf{x} \int_{-\infty}^{\infty} d\mathbf{x}'\, \mathrm{Re}\{r_0^*(\mathbf{y}-\mathbf{x}) w(\mathbf{x}) \\ &\quad \times w(-\mathbf{x}') r_1(\mathbf{B}\boldsymbol{\tau}_b - \mathbf{A}\boldsymbol{\tau}_a + \mathbf{y} - \mathbf{x}')\}, \end{aligned} \tag{32}$$

where $w(\mathbf{x}) = \mathcal{F}^{-1}\{W(\mathbf{u})\}$ is a filter function and C is a constant. We can further define

$$r_{0w}(\mathbf{y}) \triangleq \int_{-\infty}^{\infty} d\mathbf{x} r_0(\mathbf{y}-\mathbf{x}) w(\mathbf{x})$$

and

$$r_{1w}(\mathbf{y}) \triangleq \int_{-\infty}^{\infty} d\mathbf{x} r_1(\mathbf{B}\boldsymbol{\tau}_b - \mathbf{A}\boldsymbol{\tau}_a + \mathbf{y} - \mathbf{x}) w(-\mathbf{x})$$

as filtered echo fields, and write Eq. (32) as a wide-band ambiguity function Λ:[58]

$$\Lambda(\mathbf{B}, \boldsymbol{\tau}_b) = \mathrm{Re}\left\{ \int_{-\infty}^{\infty} d\mathbf{y} r_{0w}^*(\mathbf{y}) r_{1w}(\mathbf{y}) \right\}. \tag{33}$$

The view from Eq. (33) is somewhat different from Eq. (29) although the result is the same. Equation (33) suggests we should filter the 2-D echo fields and cross correlate waveforms in the six-dimensional space defined by the motion parameters B_{11}, B_{12}, B_{21}, B_{22}, τ_{b1}, τ_{b2}. The peak value of Λ gives joint ML estimates of the motion parameters such that $\mathbf{B} = \mathbf{A}$ and $\boldsymbol{\tau}_b = \boldsymbol{\tau}_a$.

B. Implementation

Least-squares techniques in elasticity imaging are common,[16,29] but are they consistent with the ML approach? The principal criterion of least-squares algorithms is to mini-

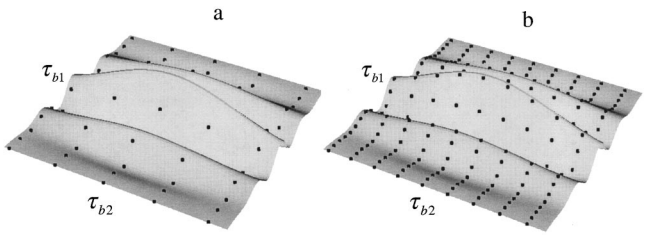

FIG. 4. Sampled ambiguity functions using (a) companding and (b) warping algorithms.

mize a matching energy function E_m. Using the filtered echo waveforms of Eq. (33), we express the matching energy as

$$E_m = \int d\mathbf{x} |r_{0w}^*(\mathbf{x}) - r_{1w}(\mathbf{x})|^2$$
$$= \int d\mathbf{x} |r_{0w}(\mathbf{x})|^2 + \int d\mathbf{x} |r_{1w}(\mathbf{x})|^2$$
$$- 2\,\mathrm{Re}\left\{ \int d\mathbf{x} r_{0w}^*(\mathbf{x}) r_{1w}(\mathbf{x}) \right\}. \quad (34)$$

The first two terms on the right side of Eq. (34) are proportional to the energy in the respective echo fields. In the absence of severe echo decorrelation, for which no algorithm can successfully estimate motion, the energy terms are approximately constant and not of interest. Minimizing the matching energy is equivalent to maximizing the third term—the wide-band ambiguity function of Eq. (33). Consequently, the ML estimator is implemented by the least-squares approach to motion estimation.

The exact ML algorithm for strain imaging would exhaustively search the relevant parameter space of the ambiguity function for the largest peak value, and thus obtain estimates for each motion parameter. Given the model of Eq. (5), there are 2 parameters that define motion in 1-D echo fields,[59] 6 parameters for 2-D echo fields, and 12 parameters for 3-D echo fields. Sampling limitations of echo fields and long computational times are practical considerations that restrict the extent of the search, so we compromise.

For example, the internal motion from a very small compression applied along the transducer beam can be approximated by 1-D translation and scaling. The optimal solution for this motion estimation problem is provided by the wide-band ML estimator for a spread target with constant displacement gradient.[34]

Larger compression produces greater strain contrast, which is desirable, but it also produces larger, more complex motion and hence poses a greater challenge to the algorithm. Normally we impose boundary conditions that confine movement to the scan plane of the linear array transducer. A block matching algorithm is used to measure local displacements in two spatial dimensions, i.e., $\mathbf{B}\boldsymbol{\tau}_b$, for each data segment (Fig. 1). The sampled waveforms are companded and then cross correlated to estimate the residual displacement $\hat{\boldsymbol{\tau}}$.[26] The nature of ultrasonic beamforming using a linear array results in echo fields that are sampled finely along x_1 and coarsely along x_2. The ambiguity function for this situation is illustrated in Fig. 4(a), where τ_{bi} is the displacement estimate along x_i obtained from block matching. Equation (33) for continuous data is represented by the shaded surface. The same values for sampled data are shown as points. In this example, sparse sampling along x_2 leads to an estimation error.

We reduce displacement estimation errors using a warping algorithm that searches for an ambiguity function peak in a sparsely sampled six-parameter space.[29] Our least-squares warping algorithm begins with the same block-matching algorithm used in companding and ends with a perturbation technique that finely tunes the block-matching estimates. Observing the same two parameters of the ambiguity function, we find in Fig. 4(b) that the perturbation component of the algorithm extends the number of sampled points about those determined using block matching. Hence we explain the reduced noise seen with warping versus companding as the consequence of a more thorough sampled ambiguity function in the plane of the displacement vector [Fig. 4(a) versus Fig. 4(b)] and a modest extension of the search to include motion parameters from the coordinate transformation matrix **B** (not shown in Fig. 4).

IV. CRAMÉR–RAO VARIANCE BOUNDS

The log-likelihood function also provides a means for determining a lower bound on estimation variance based on the information available from the data. The link between the two is the Fisher information matrix **J** with components[60]

$$J_{ii'} = -E\left\{ \frac{\partial^2 \ln p(\hat{\mathbf{R}}|\boldsymbol{\theta})}{\partial\theta_i \partial\theta_{i'}} \right\}. \quad (35)$$

The variance of an unbiased estimate $\hat{\theta}_i$ is bounded from below by

$$\mathrm{var}(\hat{\theta}_i) = E\{(\hat{\theta}_i - \theta_i)^2\} \geqslant (\mathbf{J}^{-1})_{ii}. \quad (36)$$

A. Displacement

Applying Eq. (31) to Eqs. (35) and (36) and assuming each displacement is independent of other parameters in $\boldsymbol{\theta}$, the displacement variance about the true value[61] and along x_1 is bounded by

$$\mathrm{var}(\hat{\tau}_1) = E\{(\hat{\tau}_1 - (\mathbf{A}\boldsymbol{\tau}_a - \mathbf{B}\boldsymbol{\tau}_b)_1)^2\}$$
$$\geqslant \frac{A_{12}^2 Y_1 + A_{22}^2 Y_2}{(A_{11}A_{22} - A_{12}A_{21})^2 Y_1 Y_2}. \quad (37)$$

Y_1 and Y_2 are frequency integrals (Appendix B) that summarize the effects of the pulse bandwidth and beam width on displacement variance, respectively.[62] Both are functions of the deformation parameters. Equation (37) is derived in Appendix B for two spatial dimensions where we assume $\boldsymbol{\tau}_a$ and **A** are independent. When the displacement and deformation parameters for 2-D motion are coupled, the size of **J** increases from 2×2 to 6×6, and the variance bound is reduced if information is added. Reduced variance for joint range-velocity estimation has been demonstrated.[31,34]

Equation (37) shows how object deformation and rotation reduce the information content of the echo signals with regard to displacement estimation.

1. Example 1

An incompressible medium is deformed in two dimensions by a scaling transformation, i.e., $A_{11}=A_{22}^{-1}$ and $A_{ij}=A_{ji}=0$. The corresponding variance bound is

$$\mathrm{var}(\hat{\tau}_1)\geqslant\frac{1}{A_{11}^2 Y_1}=\left(2\mathcal{S}'A_{11}^2\int_0^\infty d\mathbf{u}(2\pi u_1)^2\frac{|\gamma_{r_0r_1}(\mathbf{u})|^2}{(1-|\gamma_{r_0r_1}(\mathbf{u})|^2)}\right)^{-1}. \tag{38}$$

The same result was found in one dimension by Knapp and Carter for $A_{11}=1$.[50] Scaling increases the displacement variance directly through the factor A_{11} and indirectly by decreasing the MSC.

2. Example 2

An object is sheared either axially (along x_1) or laterally (along x_2):

$$\mathbf{A}=\begin{pmatrix}1 & A_{12}\\ 0 & 1\end{pmatrix}(\text{axial}) \quad \text{and} \quad \mathbf{A}=\begin{pmatrix}1 & 0\\ A_{21} & 1\end{pmatrix}(\text{lateral}).$$

From Eq. (37) the corresponding variance bounds are

$$\mathrm{var}(\hat{\tau}_1)\geqslant\frac{1}{Y_1}+\frac{A_{12}^2}{Y_2}(\text{axial}) \quad \text{and} \quad \mathrm{var}(\hat{\tau}_1)\geqslant\frac{1}{Y_1}(\text{lateral}). \tag{39}$$

Rotation occurs when $A_{12}=-A_{21}$. Since Y_1 and Y_2 are each functions of $\mathbf{A}$, the relative effects of each motion are not immediately obvious from Eqs. (38) and (39). We did compare variances for axial and lateral shear using simulations,[63] and found that a given amount of axial shear always produces more displacement variance than the same amount of lateral shear.[64] The largest variance for axial shear occurred with the widest ultrasound beam.

For purposes of comparison and illustration, we now examine specific examples of the scaling-only result for 1-D signal and noise sequences that are described by the bandpass white, autospectral density functions

$$G_{\bar{r}_0\bar{r}_0}(u)=G_{\bar{r}_1\bar{r}_1}(u)=G_s\left[\mathrm{rect}\left(\frac{u-u_0}{U_0}\right)+\mathrm{rect}\left(\frac{u+u_0}{U_0}\right)\right]$$

and

$$G_{n_0n_0}(u)=G_{n_1n_1}(u)=G_n\left[\mathrm{rect}\left(\frac{u-u_0}{U_0}\right)+\mathrm{rect}\left(\frac{u+u_0}{U_0}\right)\right]$$

with center frequency u_0, bandwidth U_0, and power spectral densities G_s and G_n. The value of $\mathrm{rect}((u-u_0)/U_0)$ is unity over U_0 that is centered at u_0 and zero elsewhere.

3. Example 3

With no deformation or rotation, $|\gamma_{z_0z_1}(u)|^2=1$ for all u. In addition, assume the channel signal-to-noise ratios are equal and large, $S/N_0(u)=S/N_1(u)=G_s/G_n\gg 1$, so that Eq. (19) gives $\mathrm{SNR}(u)=G_s/2G_n$. Combining Eqs. (19) and (38) we find

$$\mathrm{var}(\hat{\tau}_1)\geqslant\left(4\pi^2\mathcal{S}'\frac{G_s}{2G_n}2\int_{u_0-U_0/2}^{u_0+U_0/2}du u^2\right)^{-1}=\left(4\pi^2\mathcal{S}'\frac{G_s}{G_n}U_0u_0^2\left(1+\frac{U_0^2}{12u_0^2}\right)\right)^{-1},$$

exactly the variance bound found by numerous investigators[65] for passive radar and sonar systems[66] at high SNR and for time-independent time delay. Lacking deformation, this example is a trivial result for strain imaging.

4. Example 4

Given the assumptions above, but allowing the object function to decorrelate because of a scaling deformation, i.e., $|\gamma_{z_0z_1}(u)|^2\leqslant 1$, Eq. (38) reduces to the result of Walker and Trahey [Eq. (20) in Ref. 67]. Converting our notation to theirs, $|\gamma_{z_0z_1}(u)|^2\leftrightarrow\rho^2$, $G_s/G_n\leftrightarrow\mathrm{SNR}^2$, $\mathcal{S}'\leftrightarrow T$, $u_0\leftrightarrow(1/c_0+i\alpha_0/2\pi)2f_0$, and $U_0/u_0\leftrightarrow B$. The two sets of results are compared in Sec. VI below.

The new contribution that Eq. (37) makes to the vast existing literature on time-delay estimation is to reveal how two-dimensional motions in the object couple to increase displacement variance along one direction—that parallel to the ultrasound beam.

B. Strain

If the total displacement vector is $\mathbf{v}=\hat{\boldsymbol{\tau}}+\mathbf{B}\boldsymbol{\tau}_b$, the Eulerian strain tensor is[24]

$$\epsilon_{mn}=\frac{1}{2}\left[\frac{\partial v_n}{\partial x_m}+\frac{\partial v_m}{\partial x_n}\right]$$

and the longitudinal strain along the beam axis is

$$s\triangleq\epsilon_{11}=\frac{\partial v_1}{\partial x_1}. \tag{40}$$

In practice, however, strain is estimated from the difference equation

$$\hat{s}=\frac{v_1^{(2)}-v_1^{(1)}}{\Delta T}, \tag{41}$$

where the superscript numbers in parentheses label the positions of two displacement estimates from waveform segments along the beam that are separated by the axial distance ΔT. By error propagation,

$$\mathrm{var}(\hat{s})=\frac{(\mathrm{var}(\hat{\tau}_1^{(1)})+\mathrm{var}(\hat{\tau}_1^{(2)})-2\,\mathrm{cov}(\hat{\tau}_1^{(1)},\hat{\tau}_1^{(2)}))}{\Delta T^2}\simeq\frac{2\,\mathrm{var}(\hat{\tau}_1)}{T_1\Delta T}. \tag{42}$$

The last form makes use of a conservative approximation for the covariance[68] that was shown to be reasonably accurate.[69] The lower bound on strain error is found by combining Eqs. (37) and (42).

V. METHODS

A. Simulations

We explored the consequences of Eqs. (37) and (42) for strain imaging through the use of 2-D echo waveform simulations. Echo fields from a linear array were generated from their Fourier-domain representations, Eqs. (A3) and (A5). We set $\mathbf{B}=\mathbf{I}$ and $\boldsymbol{\tau}_a=\boldsymbol{\tau}_b=\mathbf{0}$ to isolate the effects of object deformation on displacement variance and to be consistent with the assumptions leading to Eq. (37). Quantities $z(\mathbf{x})$ and $n_j(\mathbf{x})$ were assigned samples of a Gaussian, white random process as given by $\mathcal{N}(0,S/N(\mathbf{u}_0))$ and $\mathcal{N}(0,1)$, respectively. $S/N(\mathbf{u}_0)=100$ (20 dB) for all the data. This object function simulates scattering from a medium with randomly positioned particles, each smaller than the smallest wavelength in the pulse, and with sufficient number density to produce fully developed speckle. The noise function represents electronic fluctuations and quantization errors. The 2-D point-spread function was a Gaussian-modulated sine wave

$$\tilde{h}(\mathbf{x})=(2\pi L_1 L_2)^{-1}\exp\left(-\frac{1}{2}\left(\frac{x_1^2}{L_1^2}+\frac{x_2^2}{L_2^2}\right)\right)\sin(2\pi u_0 x_1).$$

L_1 and L_2 are spatial parameters that determine the pulse length and beam width, respectively. The temporal carrier frequency of the pulse was $u_0 c_0/2=f_0=5$ MHz. The effective temporal bandwidth was computed assuming the expression[70]

$$\frac{\int_0^\infty du_1|\tilde{H}(u_1)|^2}{|\tilde{H}(u_0)|^2}=\frac{c_0}{4\sqrt{\pi}L_1}.$$

Setting $2L_1/c_0=0.1\,\mu$s gave an effective bandwidth of 2.8 MHz (56%). Including the above details into Eq. (A3) yields for two-dimensional data structures

$$R_0(u_1,u_2)=H(u_1,u_2)Z(u_1,u_2)+N_0(u_1,u_2), \tag{43}$$

where

$$H(u_1,u_2)=C' u_1^2 e^{-\alpha}\,\mathrm{sgn}(u_1)e^{-2\pi^2(|u_1|-u_0)^2L_1^2}e^{-2\pi^2u_2^2L_2^2},$$

where u_1 and u_2 are spatial-frequency variables corresponding to x_1 and x_2, respectively, and C' is a complex constant. The attenuation parameter $\alpha=2d\alpha_0|f|/20\log e$ increases linearly with temporal frequency f. The attenuation constant $\alpha_0=0.05\,\mathrm{dB\,mm^{-1}\,MHz^{-1}}$ is valid over a $d=40$ mm depth. The high-pass filtering effects of Rayleigh scattering and low-pass filtering effects of attenuation in Eq. (43) nearly cancel for Gaussian pulses, as shown in Appendix C. Although scattering and attenuation were included in these simulations, they could have been ignored without a significant loss of accuracy.

Pre-compression echo waveforms were computed using $r_0(\mathbf{x})=\mathcal{F}^{-1}\{R_0(\mathbf{u})\}$. The function $\mathrm{sgn}(u_1)=|u_1|/u_1$, $\mathrm{sgn}(0)=0$, ensures that r_0 is analytic. Post-compression echo waveforms were found in a similar manner using Eq. (A5) and the appropriate linear transformation matrix $\mathbf{A}$. Waveforms were oversampled at 400 Msamples/s along the ultrasonic beam axis to minimize errors introduced by sampling. Each waveform in the echo field was simulated assuming a lateral aperture shift of 0.18 mm. Adjacent waveforms were correlated through the Gaussian lateral beam parameter L_2 in Eq. (43) to simulate the experimental measurement conditions described below.

Displacements were measured from 5-μs segments of simulated echo data using cross correlation but *without warping* ($\mathbf{B}=\mathbf{I}$). In each case the displacement was zero ($\boldsymbol{\tau}_a=\mathbf{0}$) and the object deformation, i.e., elements of $\mathbf{A}$, were known.

B. Measurements

We also examined the efficiency of the cross correlator for displacement estimation using phantom measurements.

A 5-MHz linear array (Q2000, 5L45, 60% bandwidth, Siemens Ultrasound, Inc.) was used to scan a graphite-gelatin phantom. In the scan plane, the array was dynamically focused on receive with a constant relative aperture of $f/2$. Perpendicular to the scan plane, the focal properties were fixed at $f/4.5$ and the aperture was 10 mm. The line density of the scan plane was 4.9 A-lines/mm, so the lateral sampling interval was 0.20 mm. Echoes were recorded at 45 Msamples/s for an axial sampling interval of 0.017 mm. Each scan plane spanned approximately 40×40 mm (200 A-lines×2340 samples/A-line) and was centered at a depth of 45 mm. At the 45-mm depth, the measured lateral and elevational beam widths (−6 dB) were 0.7 mm and 1.5 mm, respectively. The correlation coefficient was 0.88 ± 0.03 between adjacent A-lines and 0.63 ± 0.05 between every third A-line.

The phantom was a graphite-gelatin block of dimensions 100 mm×100 mm×74 mm (height).[71] The block was elastically homogeneous on any scale larger than the pulse volume. It was placed on an immovable surface and compressed from above with a rigid plate in which the array transducer was flush mounted. The two side surfaces of the phantom parallel to the scan plane were restrained to prevent motion out of the plane. The remaining two phantom surfaces were free to move. All phantom surfaces were lubricated to encourage free-slip boundary conditions.

The phantom block was warmed to 21 °C, pre-loaded 4% of its 74 mm height under computer control, and electronically scanned to obtain the pre-compression echo field. It was then further compressed, held, and re-scanned at 1.2%, 2.4%, and 3.6% of its pre-loaded height (71 mm). In each case, we selected a sub-region of 50 A-lines×5.7 μs (256 pts) near the center of the echo field where there was minimal lateral motion. The pre- and post-compression waveforms were shifted to remove any time delay ($\boldsymbol{\tau}_b=\boldsymbol{\tau}_a$) but not warped ($\mathbf{B}=\mathbf{I}$). Consequently, $E\{\hat{\tau}_1\}\simeq 0$ and the deformation was predominantly axial scaling with minimal lateral scaling, shearing, or rotation. Displacement was measured for every fourth waveform in the sub-region using cross correlation. The variance $\mathrm{var}(\hat{\tau}_1)$ was computed from 16 uncorrelated echo segments 5.7 μs in duration.

The following displacement variances for simulated and experimental data represent those for unbiased, zero-mean estimates that could result from residual deformation after warping.

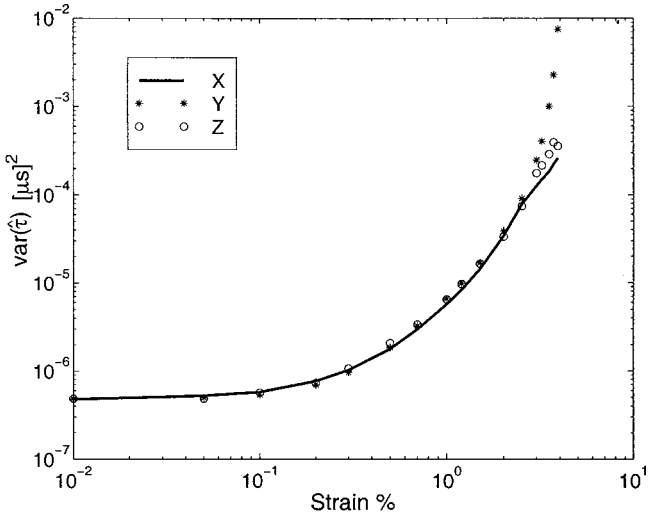

FIG. 5. Predicted displacement variances.

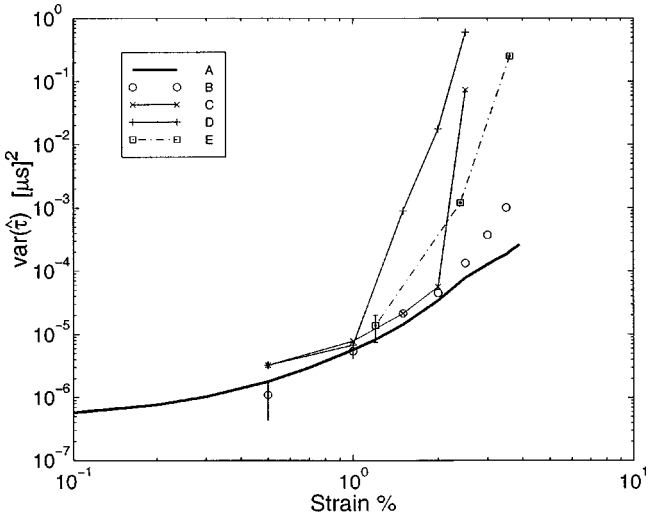

FIG. 6. Predicted versus measured displacement variances (see Sec. VI).

VI. RESULTS AND DISCUSSION

Simulated echo data provide us the means to compute the analytic predictions of Eq. (37) for arbitrary spectra and verify the results for elementary motions. Experimental echo data show us the *efficiency* of the cross correlator for displacement estimation under controlled conditions using tissuelike media and clinical ultrasonic instrumentation.

Figure 5 shows the analytic results for displacement variance as a function of the applied strain up to 4%. Simulated data were used to estimate $|\gamma_{r_0 r_1}(\mathbf{u})|^2$ for each value of applied strain. Results from 200 independent waveforms were averaged to find each point plotted. Because the deformation is limited to scaling, Eq. (38) applies. However, to facilitate comparisons with predictions from the literature, the Y_1 integral was reduced to one dimension, along u_1. Extending the frequency integral in Eq. (38) to two dimensions yields similar curves with slightly greater variances.

The open circles labeled *Z* in Fig. 5 are the results for a flat, band-pass signal spectrum and noise spectrum using Eq. (38). The asterisks labeled *Y* show the results from Walker and Trahey[67] also for flat, band-pass spectra. Values indicated by the solid line marked *X* are the results for a Gaussian echo spectrum and flat, band-pass noise spectrum using Eq. (38). Gaussian signal spectra and flat band-pass noise spectra are representative of those for strain imaging in biological media. As explained in the previous section, the channel signal-to-noise ratios at the center frequency u_0 and the effective bandwidths U_0 for the flat and Gaussian signal spectra were set equal. In general, however, the shape of the signal and noise spectra can influence the curves in Fig. 5 because SNR is a function of frequency. It is a coincidence that the variances for flat and Gaussian signal spectra coincide for realistic system and tissue parameters. The similarity of the results suggests that spectral shape is not a dominant factor determining variance for strain imaging.

The displacement variance at 0.1% strain is an important result. We routinely match scaling components of an applied strain using companding and warping methods to an average of 0.1%. Figure 5 shows that efforts to match **B** to **A** closer than 0.1% will not improve strain image noise since the precision of the cross correlator does not change below 0.1% applied strain. The precision of the cross correlator is highest in this low strain range. Assuming that ± 2 standard deviations of the displacement error is the tolerance for reliable measurements, the smallest measurable displacement at 0.1% applied strain under these typical measurement conditions is $2\sqrt{5.74\times 10^{-7}}\,\mu s^2 = 1.5$ ns or 1.2 μm. With respect to the wavelength at 5 MHz, this is less than 3° of phase!

In Fig. 6, the analytic results for the Gaussian signal spectrum shown as the solid line in Fig. 5 are reproduced as the solid line labeled A. Figure 6 results represented by the open circles labeled B are the displacement variances measured using simulated echo data for axial scaling only, $A_{11} = 1-s$. Agreement with the analytic results is nothing more than verification of programming. Results represented by $\times$labeled C and by+labeled D are variances measured using simulated echo data for axial and lateral scaling, where in C, $A_{11}=1-s$ and $A_{22}=1/2(1-s)$, and in D, $A_{11}=1-s$ and $A_{22}=1/(1-s)$. The former case represents unconstrained motion in a central plane of a homogeneous, incompressible cube. The latter case is similar but includes boundary conditions that prohibit any motion out of the plane. Decoherence from in-plane motion lateral to the beam axis increases the displacement variance by orders of magnitude. Doubling the lateral motion by adding boundary constraints halves the strain at which the sudden increase begins. Because the Cramér–Rao approach describes errors based on the information content of the waveforms, the analytic results are technique independent. Displacement variance increases with aliasing caused by undersampling the data, particularly in nonaxial directions. Aliasing errors are not reflected by Eq. (37), where we assume the data are continuous with large time-bandwidth product. The Cramér–Rao approach establishes the best-possible estimation performance and consequently the standard by which the efficiency of real estimators is measured. Our simulated echo fields were sampled at a rate of 400 Msamples/s to minimize sampling errors. Typical experimental data are sampled at much lower rates, in this case 45 Msamples/s, and interpolated.

Finally, phantom measurements are plotted in Fig. 6 at

the three values of applied strain indicated by the squares and marked E. The most remarkable feature of the experimental results is the relatively high efficiency of cross correlation for displacement estimation with 1.2% strain: The variance measured in a tissuelike phantom is only 30% larger than the lower bound. Using the two-standard deviation criteria discussed above, the data point at 1.2% applied strain shows the precision for displacement to be 7.4 ns or 5.7 μm. The predicted variance was 4.4 μm. This is the first experimental evidence to suggest that cross correlation can be an efficient estimator of ultrasonic displacement in the Cramér–Rao sense when deformation is minimized through warping. Agreement between prediction and measurement was found despite subtle differences in the parameters used to generate analytical results and phantom measurements. For the analysis, the peak frequency was 5 MHz, the bandwidth was 56%, the channel signal-to-noise ratio at the peak frequency was 20 dB, the window length was 5 μs, and the attenuation coefficient slope was 0.5 $\mathrm{dB\,cm^{-1}\,MHz^{-1}}$. For the phantom measurements the peak frequency was 4.2 MHz, the bandwidth was 60%, the channel signal-to-noise ratio at the peak frequency was 17 dB, the window length was 5.7 μs, and the attenuation slope was 0.4 $\mathrm{dB\,cm^{-1}\,MHz^{-1}}$.

VII. SUMMARY

A mathematical model is proposed to describe the ultrasonic waveforms recorded during strain imaging. From this model, the ML strategy for displacement and strain estimation is derived. In addition, a lower bound on displacement variance was found, verified using simulated echo data, and compared with experimental data obtained using a tissuelike phantom.

The ML strategy for image formation is to find the global peak of the ambiguity function. We implement an approximation to the ML strategy by filtering waveforms to favor frequency components with the highest coherence and then warping the pre-compression echo field to match the physical deformation recorded by the post-compression echo field. Finally, warped pre-compression and post-compression waveforms are cross correlated and the net displacement field is differentiated along the direction of the ultrasound beam axis to estimate strain. The ML approach to displacement and strain estimation is consistent with the generalized cross correlator, ambiguity function, and least-squares approaches described in the time-delay literature. It is possible to implement exactly only when the spectral properties of the signal and noise are known and the data are oversampled.

In most practical situations, errors predicted by the Cramér–Rao approach cannot be achieved because the assumptions of continuous echo waveforms and large time-bandwidth products are unrealistic for imaging. This variance bound ignores essential design issues relating noise, spatial resolution and aliasing. Nevertheless, the ML strategy is a rigorous, broad framework for designing systems and algorithms for strain imaging.

ACKNOWLEDGMENTS

The authors gratefully acknowledge helpful discussions with Michel Bertrand, Roch Maurice, Ed Titlebaum, Bill Walker, and Harry Barrett. This work was supported in part by the Whitaker and National Science Foundations BES 9708221.

APPENDIX A

The Fourier transforms of the echo signals $r_1(\mathbf{x})$ and $r_2(\mathbf{x})$ are derived below.

From Eq. (7),

$$r_0(\mathbf{x}) = \overline{r}_0(\mathbf{x}) + n_0(\mathbf{B}^{-1}\mathbf{x} - \boldsymbol{\tau}_b),$$

$$r_1(\mathbf{x}) = \overline{r}_1(\mathbf{x}) + n_1(\mathbf{x}).$$

Therefore,

$$\begin{aligned}
\overline{r}_0(\mathbf{x}) &= \int_{-\infty}^{\infty} d\mathbf{x}'\, h(\mathbf{B}^{-1}\mathbf{x} - \boldsymbol{\tau}_b - \mathbf{x}')\, z(\mathbf{x}') \\
&= \int_{-\infty}^{\infty} d\mathbf{x}' \left[\int_{-\infty}^{\infty} d\boldsymbol{\xi} H(\boldsymbol{\xi}) e^{i2\pi \boldsymbol{\xi}^t (\mathbf{B}^{-1}\mathbf{x} - \boldsymbol{\tau}_b - \mathbf{x}')} \right] \\
&\quad \times \left[\int_{-\infty}^{\infty} d\boldsymbol{\zeta} Z(\boldsymbol{\zeta}) e^{i2\pi \boldsymbol{\zeta}^t \mathbf{x}'} \right], \\
&= \int_{-\infty}^{\infty} d\boldsymbol{\xi} \int_{-\infty}^{\infty} d\boldsymbol{\zeta} H(\boldsymbol{\xi}) Z(\boldsymbol{\zeta}) e^{i2\pi \boldsymbol{\xi}^t (\mathbf{B}^{-1}\mathbf{x} - \boldsymbol{\tau}_b)} \\
&\quad \times \int_{-\infty}^{\infty} d\mathbf{x}' e^{i2\pi (\boldsymbol{\zeta} - \boldsymbol{\xi})^t \mathbf{x}'}.
\end{aligned} \tag{A1}$$

The integral over $\mathbf{x}'$ is $\delta(\boldsymbol{\xi} - \boldsymbol{\zeta})$. Substituting $\mathbf{u}'^t = \boldsymbol{\xi}^t \mathbf{B}^{-1}$ into Eq. (A1) and noting that $d\boldsymbol{\xi} = \det \mathbf{B}\, d\mathbf{u}'$ we find

$$\overline{r}_0(\mathbf{x}) = \det \mathbf{B} \int_{-\infty}^{\infty} d\mathbf{u}' H(\mathbf{B}^t \mathbf{u}') Z(\mathbf{B}^t \mathbf{u}') e^{i2\pi \mathbf{u}'^t (\mathbf{x} - \mathbf{B}\boldsymbol{\tau}_b)}. \tag{A2}$$

The Fourier transform of $\overline{r}_0(\mathbf{x})$ is

$$\begin{aligned}
\overline{R}_0(\mathbf{u}) &= \int_{-\infty}^{\infty} d\mathbf{x} \overline{r}_0(\mathbf{x}) e^{-i2\pi \mathbf{u}^t \mathbf{x}} \\
&= \det \mathbf{B} \int_{-\infty}^{\infty} d\mathbf{u}' H(\mathbf{B}^t \mathbf{u}') Z(\mathbf{B}^t \mathbf{u}') e^{-i2\pi \mathbf{u}'^t \mathbf{B}\boldsymbol{\tau}_b} \\
&\quad \times \int_{-\infty}^{\infty} d\mathbf{x} e^{i2\pi (\mathbf{u}' - \mathbf{u})^t \mathbf{x}} \\
&= \det \mathbf{B} H(\mathbf{B}^t \mathbf{u}) Z(\mathbf{B}^t \mathbf{u}) e^{-i2\pi \mathbf{u}^t \mathbf{B}\boldsymbol{\tau}_b},
\end{aligned}$$

and consequently

$$R_0(\mathbf{u}) = \det \mathbf{B} (H(\mathbf{B}^t \mathbf{u}) Z(\mathbf{B}^t \mathbf{u}) + N_0(\mathbf{B}^t \mathbf{u})) e^{-i2\pi \mathbf{u}^t \mathbf{B}\boldsymbol{\tau}_b}. \tag{A3}$$

Similarly, for $\overline{r}_1(\mathbf{x})$,

$$\overline{r_1}(\mathbf{x}) = \int_{-\infty}^{\infty} d\mathbf{x}' h(\mathbf{x}-\mathbf{x}') z(\mathbf{A}^{-1}\mathbf{x}' - \boldsymbol{\tau}_a)$$
$$= \int_{-\infty}^{\infty} d\mathbf{x}' \left[\int_{-\infty}^{\infty} d\boldsymbol{\xi} H(\boldsymbol{\xi}) e^{i2\pi \boldsymbol{\xi}^t(\mathbf{x}-\mathbf{x}')} \right] \times \left[\int_{-\infty}^{\infty} d\boldsymbol{\zeta} Z(\boldsymbol{\zeta}) e^{i2\pi \boldsymbol{\xi}^t(\mathbf{A}^{-1}\mathbf{x}' - \boldsymbol{\tau}_a)} \right],$$
$$= \int_{-\infty}^{\infty} d\boldsymbol{\xi} \int_{-\infty}^{\infty} d\boldsymbol{\zeta} H(\boldsymbol{\xi}) Z(\boldsymbol{\zeta}) e^{i2\pi(\boldsymbol{\xi}^t\mathbf{x} - \boldsymbol{\zeta}^t\boldsymbol{\tau}_a)} \delta(\boldsymbol{\xi} - \mathbf{A}^{-1t}\boldsymbol{\zeta}),$$
$$= \det \mathbf{A} \int_{-\infty}^{\infty} d\boldsymbol{\xi} H(\boldsymbol{\xi}) Z(\mathbf{A}^t\boldsymbol{\xi}) e^{i2\pi \boldsymbol{\xi}^t(\mathbf{x} - \mathbf{A}\boldsymbol{\tau}_a)}. \quad \text{(A4)}$$

The last form was found by noticing that the delta function is nonzero only at $\boldsymbol{\zeta} = \mathbf{A}^t\boldsymbol{\xi}$ and that $d\boldsymbol{\zeta} = \det \mathbf{A}\, d\boldsymbol{\xi}$. Finally,

$$R_1(\mathbf{u}) = \det \mathbf{A} H(\mathbf{u}) Z(\mathbf{A}^t\mathbf{u}) e^{-i2\pi \mathbf{u}^t \mathbf{A}\boldsymbol{\tau}_a} + N_1(\mathbf{u}). \quad \text{(A5)}$$

Warping the data affects all components of $R_0(\mathbf{u})$ whereas the physical deformation affects only the object function in $R_1(\mathbf{u})$.

APPENDIX B

The Fisher information component that defines the lower bound on displacement variance measured along the ultrasound beam, Eq. (37), is derived below.

We assume the displacements are independent of other parameters in $\boldsymbol{\theta}$, 2-D object motion (plane-strain state), and 2-D data structure (scan plane from a linear array). Then, from Eqs. (31) and (35),

$$-E\left\{ \frac{\partial^2 \ln p(\hat{\mathbf{R}}|\boldsymbol{\tau}_a)}{\partial \tau_{a1}^2} \right\}_{\hat{\boldsymbol{\tau}} = \mathbf{A}\boldsymbol{\tau}_a - \mathbf{B}\boldsymbol{\tau}_b}$$
$$= 4\pi^2 \mathcal{S}' \int_{-\infty}^{\infty} d\mathbf{u} \frac{|\gamma_{r_0 r_1}(\mathbf{u})|^2}{(1-|\gamma_{r_0 r_1}(\mathbf{u})|^2)} (A_{11}u_1 + A_{21}u_2)^2,$$
$$-E\left\{ \frac{\partial^2 \ln p(\hat{\mathbf{R}}|\boldsymbol{\tau}_a)}{\partial \tau_{a2}^2} \right\}_{\hat{\boldsymbol{\tau}} = \mathbf{A}\boldsymbol{\tau}_a - \mathbf{B}\boldsymbol{\tau}_b}$$
$$= 4\pi^2 \mathcal{S}' \int_{-\infty}^{\infty} d\mathbf{u} \frac{|\gamma_{r_0 r_1}(\mathbf{u})|^2}{(1-|\gamma_{r_0 r_1}(\mathbf{u})|^2)} (A_{12}u_1 + A_{22}u_2)^2,$$
$$-E\left\{ \frac{\partial^2 \ln p(\hat{\mathbf{R}}|\boldsymbol{\tau}_a)}{\partial \tau_{a1} \partial \tau_{a2}} \right\}_{\hat{\boldsymbol{\tau}} = \mathbf{A}\boldsymbol{\tau}_a - \mathbf{B}\boldsymbol{\tau}_b}$$
$$= 4\pi^2 \mathcal{S}' \int_{-\infty}^{\infty} d\mathbf{u} \frac{|\gamma_{r_0 r_1}(\mathbf{u})|^2}{(1-|\gamma_{r_0 r_1}(\mathbf{u})|^2)} (A_{11}u_1 + A_{21}u_2) \times (A_{12}u_1 + A_{22}u_2).$$

Completing the squares and integrating, we find that terms linear in frequencies u_1 and u_2 integrate to zero. Factoring the components of $\mathbf{A}$ out of the remaining integrals allows the following simplifications:

$$J_{11} = A_{11}^2 Y_1 + A_{21}^2 Y_2,$$
$$J_{22} = A_{12}^2 Y_1 + A_{22}^2 Y_2,$$
$$J_{12} = J_{21} = A_{11}A_{12}Y_1 + A_{21}A_{22}Y_2,$$

where

$$Y_1 \triangleq 2\mathcal{S}' \int_0^{\infty} d\mathbf{u} (2\pi u_1)^2 \frac{|\gamma_{r_0 r_1}(\mathbf{u})|^2}{(1-|\gamma_{r_0 r_1}(\mathbf{u})|^2)},$$
$$Y_2 \triangleq 2\mathcal{S}' \int_0^{\infty} d\mathbf{u} (2\pi u_2)^2 \frac{|\gamma_{r_0 r_1}(\mathbf{u})|^2}{(1-|\gamma_{r_0 r_1}(\mathbf{u})|^2)}. \quad \text{(B1)}$$

The determinant of the Fisher information matrix is

$$\det \mathbf{J} = (A_{11}A_{22} - A_{12}A_{21})^2 Y_1 Y_2.$$

Finally, we arrive at Eq. (37):

$$\text{var}(\hat{\tau}_1) \geqslant (\mathbf{J}^{-1})_{11} = \frac{A_{12}^2 Y_1 + A_{22}^2 Y_2}{(A_{11}A_{22} - A_{12}A_{21})^2 Y_1 Y_2}.$$

APPENDIX C

We show that the sensitivity function for a Gaussian point-spread function is approximately Gaussian. The function

$$H(f, f_0, \sigma) = C' |f|^m e^{-\alpha} \text{sgn}(f) e^{-2\pi^2 (|f| - f_0)^2 \sigma^2},$$
$$f_0, \sigma, \alpha > 0, \quad \text{(C1)}$$

is a 1-D temporal-frequency representation of the sensitivity function described by Eq. (43). The high-pass factor $|f|^m$ defines the scattering function, where $0 \leqslant m \leqslant 2$, $m = 0$ is for specular reflection, and $m = 2$ is for Rayleigh scattering; the low-pass factor $\exp(-\alpha)$ defines attenuation losses; the remainder represents the point-spread function of a Gaussian-modulated sine wave with center frequency f_0 and pulse duration σ.

We find that

$$H(f, f_1, \sigma_1) = C_1 \text{sgn}(f) e^{-2\pi^2 (|f| - f_1)^2 \sigma_1^2}$$
$$= \lim_{\sigma \to \infty} H(f, f_1, \sigma), \quad \text{(C2)}$$

where the constants

$$C_1 = C' f_1^m e^{-\alpha} e^{-2\pi^2 (f_1 - f_0)^2 \sigma^2},$$
$$f_1 = \frac{-\alpha + 4\pi^2\sigma^2 f_0 + \sqrt{16\pi^2\sigma^2 m + (\alpha - 4\pi^2\sigma^2 f_0)^2}}{8\pi^2\sigma^2},$$

and

$$\sigma_1 = \sigma \frac{f_1^2 e^{-\alpha(f_1 - f_0)} e^{-\alpha^2/8\pi^2\sigma^2} e^{-2\pi^2 (f_1 - f_0)^2 \sigma^2}}{\frac{1}{4\pi^2\sigma^2}\left(1 + \frac{\alpha^2}{4\pi^2\sigma^2}\right) - f_0 \frac{\alpha}{2\pi^2\sigma^2} + f_0^2}.$$

That is, for narrow-band transmission, the sensitivity function is Gaussian with $\sigma_1 \simeq \sigma$ and f_1 given above. It is also a very good approximation for broadband transmission. For example, let $f_0 = 5$ MHz, $\sigma = 0.1$ μs (effective bandwidth $= 2.8$ MHz), $m = 2$, and $\alpha = 2.3$ [$= 0.05$ dB/mm/MHz $\times (2 \times 40$ mm$) \times 5$ MHz$/(20 \log e)$]. We find that $f_1/f_0 = 0.97$, $\sigma_1/\sigma = 1.11$, and $|H(f, f_0, \sigma) - H(f, f_1, \sigma_1|/C_1 < 0.026$. Consequently, we may use a 1-D Gaussian sensitivity function when the 1-D point-spread function is Gaussian without significant error. The situation can be more complicated when modeling the point spread function at higher spatial dimensions.

[1] L. S. Wilson and D. E. Robinson, Ultrason. Imaging **4**, 71 (1982).
[2] R. J. Dickinson and C. R. Hill, Ultrasound Med. Biol. **8**, 263 (1982).
[3] M. Tristam *et al.*, Ultrasound Med. Biol. **12**, 927 (1986).
[4] T. A. Krouskop, D. Dougherty, and S. F. Levinson, J. Rehabil. Res. Dev. **24**, 1 (1987).
[5] K. A. Wear and R. L. Popp, IEEE Trans. Ultrason. Ferroelectr. Freq. Control **34**, 368 (1987).
[6] R. Adler, J. Rubin, P. Bland, and P. Carson, Ultrasound Med. Biol. **16**, 561 (1990).
[7] P. DeJong, T. Arts, A. Hoeks, and R. Reneman, Ultrason. Imaging **12**, 84 (1990).
[8] Y. Yamakoshi, J. Sato, and T. Sato, IEEE Trans. Ultrason. Ferroelectr. Freq. Control **37**, 45 (1990).
[9] R. Lerner, S. Huang, and K. Parker, Ultrasound Med. Biol. **16**, 231 (1990).
[10] I. Céspedes, J. Ophir, H. Ponnekanti, Y. Yazdi, and X. Li, Ultrason. Imaging **15**, 73 (1993).
[11] M. O'Donnell, A. Skovoroda, B. Shapo, and S. Emelianov, IEEE Trans. Ultrason. Ferroelectr. Freq. Control **41**, 314 (1994).
[12] K. Raghavan and A. Yagle, IEEE Trans. Nucl. Sci. **41**, 1639 (1994).
[13] S. Emelianov, A. Skovoroda, M. Lubinski, and M. O'Donnell, Acoust. Imaging **21**, 241 (1995).
[14] C. Sumi, A. Suzuki, and K. Nakayama, IEEE Trans. Biomed. Eng. **42**, 193 (1995).
[15] E. Chen, R. Adler, P. Carson, W. Jenkins, and W. O'Brien, Ultrasound Med. Biol. **21**, 1153 (1995).
[16] F. Kallel and M. Bertrand, IEEE Trans. Med. Imaging **15**, 299 (1996).
[17] M. Fatemi and J. F. Greenleaf, Science **280**, 82 (1998).
[18] K. Nightingale, R. Nightingale, T. J. Hall, and G. E. Trahey, Ultrason. Imaging **20**, 62 (1998) (abstract only).
[19] L. Axel and L. Dougherty, Radiology **171**, 841 (1989).
[20] E. R. McVeigh and E. A. Zerhouni, Radiology **180**, 677 (1991).
[21] R. Muthupillai *et al.*, Science **269**, 1854 (1995).
[22] D. Plewes, I. Betty, S. Urchuk, and I. Soutar, J. Magn. Reson Imaging **5**, 733 (1995).
[23] T. Chenevert, A. Skovoroda, M. O'Donnell, and S. Emelianov, Magn. Reson. Med. **39**, 482 (1998).
[24] Y. Fung, *Biomechanics: Mechanical Properties of Living Tissues*, 2nd ed. (Springer-Verlag, New York, 1993).
[25] C. H. Knapp and G. C. Carter, J. Acoust. Soc. Am. **61**, 1545 (1977).
[26] P. Chaturvedi, M. F. Insana, and T. J. Hall, IEEE Trans. Ultrason. Ferroelectr. Freq. Control **45**, 179 (1998).
[27] R. L. Maurice and M. Bertrand, IEEE Trans. Med. Imaging **18**, 593 (1999).
[28] F. Yeung, S. F. Levinson, D. Fu, and K. J. Parker, IEEE Trans. Med. Imaging **17**, 945 (1998).
[29] Y. Zhu, P. Chaturvedi, and M. F. Insana, Ultrason. Imaging **21**, 127 (1999).
[30] T. Varghese, J. Ophir, and I. Céspedes, Ultrasound Med. Biol. **22**, 1043 (1996).
[31] H. L. VanTrees, *Detection, Estimation and Modulation Theory, Part III* (Wiley, New York, 1971), pp. 9–22, 170–175.
[32] G. C. Carter, *Coherence and Time Delay Estimation* (IEEE Press, Piscataway, NJ, 1993).
[33] M. Azimi and A. C. Kak, Ultrason. Imaging **7**, 1 (1985).
[34] K. W. Ferrara and V. R. Algazi, IEEE Trans. Ultrason. Ferroelectr. Freq. Control **38**, 1 (1991).
[35] P. M. Morse and K. U. Ingard, *Theoretical Acoustics* (McGraw-Hill, New York, 1968), p. 427.
[36] A. Macovski, Proc. IEEE **67**, 484 (1979).
[37] Ordinarily, the magnitude of the spatial frequency variable $u=|\mathbf{u}|$ is $2f/c_0$ in mm^{-1}, where f is the temporal frequency variable in MHz and c_0 is the mean longitudinal sound speed in mm/μs. Only when it is necessary to include acoustic attenuation explicitly in the analysis will we define u as a complex variable: $u=((1/c_0)+i(\alpha_0/2\pi))2f$, where α_0 is an attenuation constant measured in $\mathrm{mm}^{-1}\,\mathrm{MHz}^{-1}$.
[38] M. F. Insana and D. G. Brown, ''Acoustic scattering theory applied to soft biological tissues,'' in *Ultrasonic Scattering in Biological Tissues*, edited by K. K. Shung and G. A. Thieme (CRC Press, Boca Raton, 1993), pp. 75–124.
[39] R. N. Bracewell, *The Fourier Transform and Its Applications*, 2nd ed. (McGraw-Hill, New York, 1978), p. 117.
[40] F. Kallel, M. Bertrand, and J. Meunier, IEEE Trans. Ultrason. Ferroelectr. Freq. Control **41**, 105 (1994).
[41] The set $\mathcal{S}$ is taken to be a Cartesian product of intervals, i.e., $\mathcal{S}=\mathcal{S}_1\times\mathcal{S}_2\times\mathcal{S}_3$, where $\mathcal{S}_i=\{y:-T_i/2\leqslant y\leqslant T_i/2, y\in\Re\}$. With this definition $\mathcal{S}'\triangleq\int_{\mathcal{S}}d\mathbf{x}=T_1T_2T_3$.
[42] Throughout the paper, $E\{\psi\}$ represents $E\{\psi\}_{z,n}=\int dz\, dnp(z,n)\psi$. However, where explicitly noted, expectations are taken over one random variable while holding the others fixed. For example, $\overline{r}(\mathbf{x})=E\{r(\mathbf{x})\}_{n|z}=\int dnp(n|z)r(\mathbf{x})$.
[43] M. Bilgen and M. F. Insana, J. Acoust. Soc. Am. **99**, 3212 (1996).
[44] M. F. Insana, P. Chaturvedi, T. J. Hall, and M. Bilgen, Proc IEEE Ultrason Symp **97CH36118**, 1435 (1997).
[45] H. H. Barrett, J. N. Aarsvold, and T. J. Roney, ''Null functions and eigenfunctions: Tools for the analysis of imaging systems,'' in *Progress in Clinical and Biological Research*, edited by D. Ortendahl and J. Llacer, Vol. 363 (1989 Information Processing in Medical Imaging Conference Proceedings, New York, 1991), pp. 211–226.
[46] M. Bilgen and M. F. Insana, IEEE Trans. Signal Process. **46**, 2589 (1998).
[47] A. Papoulis, *The Fourier Integral and Its Applications* (McGraw-Hill, New York, 1962).
[48] H. H. Barrett, J. L. Denny, R. F. Wagner, and K. J. Myers, J. Opt. Soc. Am. **12**, 834 (1995).
[49] The index k is a function of (k_1,k_2,k_3) such that $k>k'$ implies $|\mathbf{u}_k|\geqslant|\mathbf{u}_{k'}|$. Also, $u_{1k}=k_1/T_1$, $u_{2k}=k_2/T_2$, and $u_{3k}=k_3/T_3$. Since $r_j(\mathbf{x})$ is real, then $\hat{R}_{jk}=\hat{R}^*_{jk'}$ if $\mathbf{u}_k=-\mathbf{u}_{k'}$.
[50] C. H. Knapp and G. C. Carter, IEEE Trans. Acoust. Speech, Signal Process. **24**, 320 (1976).
[51] V. H. MacDonald and P. M. Schultheiss, J. Acoust. Soc. Am. **46**, 37 (1969).
[52] G. C. Carter, C. H. Knapp, and A. H. Nuttall, IEEE Trans. Audio Electroacoust. **21**, 337 (1973).
[53] H. Urkowitz, *Signal Theory and Random Processes* (Artech House, Norwood, MA, 1983).
[54] At $k=k'$, $\int_{-\infty}^{\infty}dx(\sin\pi xT/\pi xT)(\sin\pi xT/\pi xT)=(1/\pi^2T^2)\pi\min\{\pi T,\pi T\}=1/T$. See I. S. Gradshteyn, I. M. Ryzhik, and A. Jeffrey, *Table of Integrals, Series, and Products, 5/e* (Academic, San Diego, 1994), Eq. 3.741.3.
[55] E. Weinstein and A. J. Weiss, IEEE Trans. Acoust. Speech, Signal Process. **32**, 1064 (1984).
[56] S. M. Kay, *Fundamentals of Statistical Signal Processing: Estimation Theory* (PTR Prentice Hall, Englewood Cliffs, NJ, 1993), Chaps. 7 and 15.
[57] J. L. Melsa and D. L. Cohn, *Decision and Estimation Theory* (McGraw-Hill, New York, 1978), pp. 180–182.
[58] Q. Jin, K. M. Wong, and Z.-Q. Luo, IEEE Trans. Signal Process. **43**, 904 (1995).
[59] M. Bilgen, M. F. Insana, and L. T. Cook, Proceedings of the IEEE Symposium Time Frequency and Time Scale Analy (1998), pp. 65–68.
[60] H. L. VanTrees, *Detection, Estimation and Modulation Theory, Part I* (Wiley, New York, 1968).
[61] Displacement estimates are generally biased (Ref. 46). However, by examining the variance of estimates about the true value, which is the case when $\mathbf{A}\simeq\mathbf{B}$ and $\boldsymbol{\tau}_a\simeq\boldsymbol{\tau}_b$, bias may be ignored.
[62] R. N. McDonough and A. D. Whalen, *Detection of Signals in Noise*, 2nd ed. (Academic, San Diego, 1995), pp. 409–422.
[63] M. Bilgen, M. F. Insana, T. J. Hall, and M. Bertrand, Ultrason. Imaging **20**, 60 (1998) (abstract only).
[64] R. L. Maurice and M. Bertrand, IEEE Trans. Ultrason. Ferroelectr. Freq. Control **46**, 584 (1999).
[65] A. H. Quazi, IEEE Trans. Acoust. Speech, Signal Process. **29**, 527 (1981).
[66] Quazi (Ref. 65) defines a *passive* system for localization as one that compares two echo-signal measurements. An *active* system locates targets by matched filtering one echo-signal with the transmitted pulse.
[67] W. F. Walker and G. E. Trahey, IEEE Trans. Ultrason. Ferroelectr. Freq. Control **42**, 301 (1995).
[68] I. Céspedes, M. F. Insana, and J. Ophir, IEEE Trans. Ultrason. Ferroelectr. Freq. Control **42**, 969 (1995).
[69] M. Bilgen, M. F. Insana, T. J. Hall, and P. Chaturvedi, Ultrason. Imaging **19**, 209 (1997).
[70] K. S. Shanmugan and A. M. Breipohl, *Random Signals: Detection, Estimation, and Data Analysis* (Wiley, New York, 1988), pp. 146–148.
[71] T. J. Hall, M. Bilgen, M. F. Insana, and T. A. Krouskop, IEEE Trans. Ultrason. Ferroelectr. Freq. Control **44**, 1355 (1997).